Front. Phys. 10(5), 106401 (2015)
DOI 10.1007/s11467-015-0498-5

REVIEW ARTICLE

Quantum phase transitions in two-dimensional strongly correlated fermion systems

An Bao (保安)[1,3,†], **Yao-Hua Chen** (陈耀华)[2], **Heng-Fu Lin** (林恒福)[2], **Hai-Di Liu** (刘海迪)[2],
Xiao-Zhong Zhang (章晓中)[1]

[1] *Laboratory of Advanced Materials, School of Materials Science and Engineering, Tsinghua University, Beijing 100084, China*
[2] *Beijing National Laboratory for Condensed Matter Physics, Institute of Physics, Chinese Academy of Sciences, Beijing 100190, China*
[3] *Key Laboratory of Integrated Exploitation of Bayan-Obo Multi-Metal Resources, Inner Mongolia University of Science & Technology, Baotou 014010, China*
Corresponding author. E-mail: † *baoan204@aliyun.com*

Received July 13, 2015; accepted August 2, 2015

In this article, we review our recent work on quantum phase transition in two-dimensional strongly correlated fermion systems. We discuss the metal–insulator transition properties of these systems by calculating the density of states, double occupancy, and Fermi surface evolution using a combination of the cellular dynamical mean-field theory (CDMFT) and the continuous-time quantum Monte Carlo algorithm. Furthermore, we explore the magnetic properties of each state by defining magnetic order parameters. Rich phase diagrams with many intriguing quantum states, including antiferromagnetic metal, paramagnetic metal, Kondo metal, and ferromagnetic insulator, were found for the two-dimensional lattices with strongly correlated fermions. We believe that our results would lead to a better understanding of the properties of real materials.

Keywords quantum phase transition, two-dimensional lattices, fermions, cellular dynamical mean-field theory, continuous-time quantum Monte Carlo

PACS numbers 64.70.Tg, 73.20.At, 75.90.+w

Contents

1 Introduction

An important goal of condensed matter physics is to find new phases or states. Therefore, the study of quantum phase transitions in strongly correlated systems plays a vital role in condensed matter physics [1–12]. Two-dimensional lattices of strongly correlated fermions are valuable objects in condensed matter physics because of their unique properties, which attract great interest and lead to the finding of intriguing phenomena [13–25]. In addition to the popular triangular lattice, the square lattice, and the hexagonal lattice, other two-dimensional lattices include the triangular Kagomé lattice [26–29], the decorated honeycomb lattice [30, 31], the Shastry–Sutherl and lattice, and the square–octagon lattice [32–34]. The triangular Kagomé lattice was found in a new class of two-dimensional materials, $Cu_9X_2(cpa)_6\cdot xH_2O$ (where cpa = 2-carboxypentonic acid, a derivative of ascorbic acid, andX = F, Cl, Br), in which Cu spins form the geometrically frustrated lattice [35, 36]. The decorated honeycomb lattice was discovered in many synthesized nanomaterials, including the triangular organic material κ-BEDT$(CN)_3$ [37], the Kagomé lattice-structured Herberts mithite [38], and the three-dimensional hyper-Kagomé lattice magnet ($Na_4Ir_3O_8$) [39]. A two-dimensional lattice filled with Cu^{2+} ions that is topologically equivalent to the Shastry–Sutherl and lattice was found in $SrCu_2(BO_3)_2$ [40], and the quasi-square–octagon lattice was found in the functional material ZnO [41, 42]. Thus, investigations of quantum phase transitions in two-dimensional strongly correlated fermion systems not only are valuable in theoretical research but also are important for material applications.

Band theory cannot be used to describe the properties of strongly correlated systems because of the magnitude of their interactions, which is comparable to kinetic energy. Therefore, there have been many theoretical and experimental studies on two-dimensional strongly correlated fermion systems with interesting results. In this article, we review our recent work on quantum phase transitions in two-dimensional strongly correlated fermion systems, including the triangular Kagomé lattice [28], the decorated honeycomb lattice [43], the Shastry–Sutherl and lattice [31], and the square–octagon lattice [32–34], that we investigated by combining cellular dynamical mean-field theory (CDMFT) and the continuous-time quantum Monte Carlo algorithm.

2 Methods

2.1 Cellular dynamical mean-field theory

CDMFT [44–53] is a natural extension of single-site dynamical mean-field theory and a coarse graining method that maps the lattice problem onto a cluster impurity model. CDMFT can describe short-range spatial correlation exactly (local degrees of freedom to the size of a cluster) and uses effective self-consistent field (Weiss field) to describe the remaining degrees of freedom. It is important to separate the three basic elements of the CDMFT scheme. First is the degree of freedom of a cluster, which is expressed by an impurity's degree of freedom in a self-consistent field. The embedded cluster in a Weiss field leads to a cluster Green's function and a cluster self-energy. Second is the use of cluster Green's function or cluster self-energy to express a Weiss field (i.e., self-consistent condition for cluster scheme). Third is the relationship between cluster self-energy and lattice self-energy. An impurity solver can estimate cluster's local correlation, and cluster self-energy can embody lattice self-energy by using the lattice's periodicity. Using a two-dimensional square lattice as an example, in CDMFT, the lattice problem is mapped onto a cluster impurity model in which four sites are included in one cluster, as shown in Fig. 1 (we labeled the selected cluster $j = 0$).

In a grand canonical ensemble, the partition function for the system is

$$\mathcal{Z} = \int \prod_{j,\mu,\sigma} \mathcal{D}c_{i\sigma}^{\dagger} \mathcal{D}c_{i\sigma} \mathrm{e}^{-S}, \tag{1}$$

where $c_{i\sigma}^{\dagger}$ and $c_{i\sigma}$ represent particle's creation and annihilation operators respectively and σ is spin index. $\mathcal{D}$ is Grassmann variables. σ

Thus, the system's action can be defined as

$$\begin{aligned} S &= \int_0^{\beta} \mathrm{d}\tau \left(\sum_{i\mu,jv} c_{i\mu}^{\dagger} O_{\mu v}^{ij} \partial_{\tau} c_{i\mu} - H[c_{i\mu}^{\dagger}, c_{jv}] \right) \\ &\equiv S_c + S_{cb} + S_b, \end{aligned} \tag{2}$$

where i, j are cluster labels, μ, v are site labels in each cluster, action S_c is for all terms in the cluster, action S_b is for all terms excluding the cluster, and action S_{bc} connects the cluster and the self-consistent field. And τ, β, H represents time, inverse of temperature, Hamiltonian respectively, while O is a matrix which summarizes the nonorthogonality of the wave function basis. By computing the path integral for all variables, $c_{j\mu}(c_{j\mu}^{\dagger})(j \neq 0)$, we obtain the effective action for the cluster variable $c_{0\mu}(c_{0\mu}^{\dagger})$,

$$\frac{1}{\mathcal{Z}_{\mathrm{eff}}} \mathrm{e}^{-S_{\mathrm{eff}}[c_{0\mu\sigma}^{\dagger}, c_{0\mu\sigma}]} \equiv \frac{1}{\mathcal{Z}} \int \prod_{j \neq 0,\mu,\sigma} Dc_{j\mu\sigma}^{\dagger} Dc_{j\mu\sigma} \mathrm{e}^{-S}, \tag{3}$$

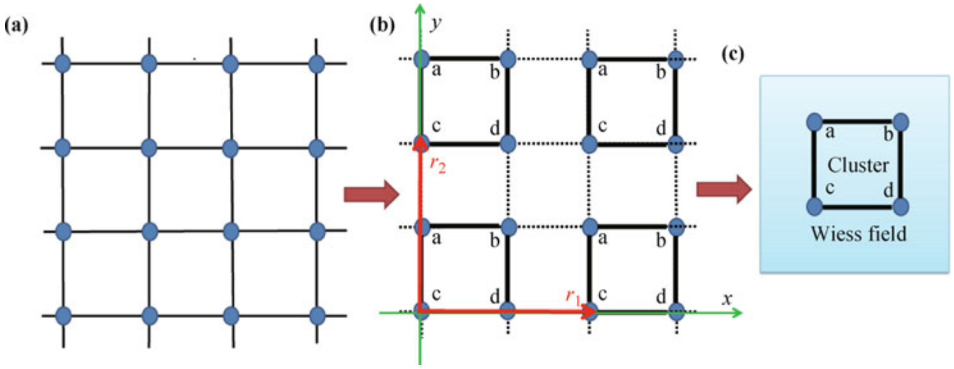

Fig. 1 **(a)** Sketch map of two dimensional square lattices before mapped onto impurity model. **(b)** Mapping square lattice problem onto cluster impurity where $N_c = 4$. **(c)** Sketch map of cluster for two dimensional square lattices after mapped onto impurity model.

$$S_{\text{eff}} = -\int_0^\beta \mathrm{d}\tau\mathrm{d}\tau' \sum_{\mu\upsilon\sigma} c^\dagger_{\mu\sigma}(\tau)\mathcal{G}^{-1}_{0,\mu\upsilon\sigma}(\tau-\tau')c_{\mu\sigma}(\tau') + \int_0^\beta \sum_{\mu=1}^{N\mathrm{c}} U n_{\mu\uparrow}(\tau)n_{\mu\downarrow}(\tau), \tag{4}$$

where $\hat{\mathcal{G}}^{-1}_{0,\mu\upsilon\sigma}(\tau-\tau')$ is the Weiss field and $\mu,\upsilon = 1,\cdots,N\mathrm{c}$ are site labels in the cluster. Cluster Green's function $G^{\mathrm{c}}_{\mu\upsilon}(\tau-\tau') \equiv -\langle T_\tau c^\dagger_\mu(\tau)c_\upsilon(\tau')\rangle$ and self-energy $\hat{\sum}^{c}_{\mu\upsilon}(\mathrm{i}\omega_n) \equiv \mathcal{G}^{-1}_{\mu\upsilon}(\mathrm{i}\omega_n) - G^{c^{-1}}_{\mu\upsilon}(\mathrm{i}\omega_n)$ are obtained from the effective action S_{eff}, in which the degree of freedom of spin is omitted. A new Weiss field can be obtained from the Dyson equation:

$$\mathcal{G}_0^{-1}(\mathrm{i}\omega_n) = \left[\sum_K \frac{1}{(\mathrm{i}\omega_n+\mu)\hat{1} - \hat{t}(K) - \hat{\sum}^{c}(\mathrm{i}\omega_n)}\right]^{-1} + \hat{\sum}^{c}(\mathrm{i}\omega_n), \tag{5}$$

where K is the reduced Brillouin zone, $\hat{1}$ is a 4×4 unit matrix, μ is the chemical Potential, $\hat{\sum}^{c}(\mathrm{i}\omega_n)$ is the cluster self-energy, which is a 4×4 matrix, and $\hat{t}(K)$ is the 4×4 hopping matrix of the super lattice whose elements are

$$t_{ij}(K) = \sum_{\vec{r}_1-\vec{r}_2} t^{\vec{r}_1\vec{r}_2}_{ij} \exp[iK\cdot(\vec{r}_1-\vec{r}_2)],$$

where $\vec{r}_1$ and $\vec{r}_2$ are basic vectors of the super lattice and i, j are indexes of sites in the cluster.

2.2 Continuous-time quantum Monte Carlo algorithm

The continuous-time quantum Monte Carlo (CTQMC) [54–57] algorithm is used as an impurity solver for investigations on quantum phase transitions in two-dimensional lattices of strongly correlated fermions. The main mathematical methods used in the CTQMC algorithm are Metropolis sampling, the law of large numbers, and the central-limit theorem. We use the Hubbard model [58–63] as an example to introduce the CTQMC algorithm:

$$H = -t\sum_{\langle i,j\rangle\sigma}(C^\dagger_{i\sigma}C_{j\sigma} + \mathrm{h.c}) + \sum_{ij\sigma\sigma'} u_{ij}n_{i\sigma}n_{j\sigma'} + \mu\sum_i C^\dagger_{i\sigma}C_{i\sigma}, \tag{6}$$

where u stands for interaction and n represents the density operator. With respect to the interaction picture, the Hamiltonian can be written as $H = H_0 + H_1$, where H_0 is the time-independent part and H_1 is the perturbative part. Therefore, the system's partition function is

$$\mathcal{Z} = \mathrm{tr}[\exp(-\beta H)] = \mathrm{tr}T_\tau[\exp(-\beta H_0)\cdot S(\beta)], \tag{7}$$

where

$$H_1(\tau) = \mathrm{e}^{\tau H_0}H_1\mathrm{e}^{-\tau H_0} = \sum_{ij\sigma\sigma'} u_{ij}\mathrm{e}^{\tau H_0}n_{i\sigma}\mathrm{e}^{-\tau H_0}n_{j\sigma'} = \sum_{ij\sigma\sigma'} u_{ij}n_{i\sigma}(\tau)n_{j\sigma'}(\tau)$$

and $S(\beta) = T\tau\exp[-\int_0^\beta H_1(\tau)\mathrm{d}\tau]$.

After a series expansion of the system action, the system's partition function is

$$\begin{aligned}\mathcal{Z} &= \mathrm{tr}[\exp(-\beta H_0)\cdot S(\beta)]\\ &= \mathrm{tr}\{\exp(-\beta H_0)\cdot T\tau\exp[-\int_0^\beta \mathrm{d}\tau H_1(\tau)]\}\\ &= \mathrm{tr}\{\exp(-\beta H_0)\sum_k \frac{(-1)^k}{k!}\int \mathrm{d}\tau_1\int\mathrm{d}\tau_2\ldots\\ &\quad\times\int\mathrm{d}\tau_k T\tau[H_1(\tau_1)H_1(\tau_2)\cdots H_1(\tau_k)]\}\\ &= \mathrm{tr}\{\exp(-\beta H_0)\sum_k\frac{(-U)^k}{k!}\int\mathrm{d}\tau_1\ldots\\ &\quad\times\int\mathrm{d}\tau_k T\tau[\sum_{i_1} n_{i_1\uparrow}(\tau_1)n_{i_1\downarrow}(\tau_1)\cdots\\ &\quad\times\sum_{i_k} n_{i_k\uparrow}(\tau_{kl})n_{i_k\downarrow}(\tau_k)]\},\end{aligned} \tag{8}$$

where "tr" indicates the matrix trace and T_τ is a time-ordering operator. In general, the special index and the series expansion index are expressed as $\kappa \equiv \{k, i, \{\tau_i\}\}$ while there is no confusion, so the system's partition function is now

$$\mathcal{Z} = \mathcal{Z}_0\sum_\kappa\frac{(-U)^\kappa}{\kappa!}\int\mathrm{d}1\ldots\int\mathrm{d}\kappa\langle T_\tau n_\uparrow(1)\cdots n_\uparrow(\kappa)\rangle_0 \times\langle T_\tau n_\downarrow(1)\cdots n_\downarrow(\kappa)\rangle_0, \tag{9}$$

where $\mathcal{Z}_0 = \mathrm{tr}[\exp(-\beta H_0)]$. Therefore, the mean value of every observable is expressed as

$$\langle O\rangle_0 = \frac{\mathrm{tr}[\exp(-\beta H_0)]\cdot O}{\mathrm{tr}[\exp(-\beta H_0)]}. \tag{10}$$

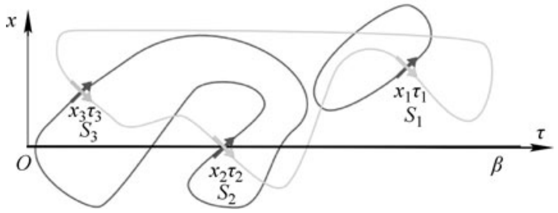

Fig. 2 Sketch map of random walk for $\kappa = 3$.

The integrand in the partition function in Eqs. (2)–(9) can be simplified by using Wick's theorem and performing a random walk for $\kappa = 3$, Fig. 2 is a scheme for random walk for $\kappa = 3$. For example, the mean value of the integrand in the partition function for the spin-up case is

$$\begin{aligned}
&\langle T_\tau n_\uparrow(1) n_\uparrow(2)\rangle_0 \\
&\quad = \left\langle T_\tau c_\uparrow^\dagger(1) c_\uparrow(1) c_\uparrow^\dagger(2) c_\uparrow(2) c_\uparrow^\dagger(3) c_\uparrow(3)\right\rangle_0 \\
&\quad = \mathcal{G}_\uparrow^0(1,1)\mathcal{G}_\uparrow^0(2,2) - \mathcal{G}_\uparrow^0(2,1)\mathcal{G}_\uparrow^0(1,2) \\
&\quad = \begin{vmatrix} \mathcal{G}_\uparrow^0(1,1) & \mathcal{G}_\uparrow^0(1,2) & \mathcal{G}_\uparrow^0(1,3) \\ \mathcal{G}_\uparrow^0(2,1) & \mathcal{G}_\uparrow^0(2,2) & \mathcal{G}_\uparrow^0(2,3) \\ \mathcal{G}_\uparrow^0(3,1) & \mathcal{G}_\uparrow^0(3,2) & \mathcal{G}_\uparrow^0(3,3) \end{vmatrix}. \qquad (11)
\end{aligned}$$

For the spin-up κ-order case,

$$\begin{aligned}
&\langle T_\tau n_\uparrow(1) n_\uparrow(2)\cdots n_\uparrow(\kappa)\rangle_0 \\
&\quad = \begin{vmatrix} \mathcal{G}_\uparrow^0(1,1) & \mathcal{G}_\uparrow^0(1,2) & \cdots & \mathcal{G}_\uparrow^0(1,\kappa) \\ \mathcal{G}_\uparrow^0(2,1) & \mathcal{G}_\uparrow^0(2,2) & \cdots & \mathcal{G}_\uparrow^0(\kappa,\kappa) \\ \vdots & \vdots & \vdots & \vdots \\ \mathcal{G}_\uparrow^0(\kappa,1) & \mathcal{G}_\uparrow^0(\kappa,2) & \cdots & \mathcal{G}_\uparrow^0(\kappa,\kappa) \end{vmatrix} \\
&\quad = \det D_\uparrow(\kappa). \qquad (12)
\end{aligned}$$

For the spin-down κ-order case, the process is the same as for spin-up and result is

$$\begin{aligned}
&\langle T_\tau n_\downarrow(1) n_\downarrow(2)\cdots n_\downarrow(\kappa)\rangle_0 \\
&\quad = \begin{vmatrix} \mathcal{G}_\downarrow^0(1,1) & \mathcal{G}_\downarrow^0(1,2) & \cdots & \mathcal{G}_\downarrow^0(1,\kappa) \\ \mathcal{G}_\downarrow^0(2,1) & \mathcal{G}_\downarrow^0(2,2) & \cdots & \mathcal{G}_\downarrow^0(\kappa,\kappa) \\ \vdots & \vdots & \vdots & \vdots \\ \mathcal{G}_\downarrow^0(\kappa,1) & \mathcal{G}_\downarrow^0(\kappa,2) & \cdots & \mathcal{G}_\downarrow^0(\kappa,\kappa) \end{vmatrix} \\
&\quad = \det D_\downarrow(\kappa), \qquad (13)
\end{aligned}$$

where $\mathcal{G}^0$ is Green's function, which corresponds to the Hamiltonian with $U = 0$.

In the CTQMC algorithm, we use the Metropolis selective sampling algorithm to generate configuration space that satisfies the target distribution density function. Adding or subtracting vertices help to realize the random walk between arbitrary configurations. For example, suppose that the lattice model has N sites and the initial configuration is k.

1) When a vertex is inserted, the new configuration is $k+1$. The probability of choosing any one spatial site is $1/N$, and the probability of extracting one vertex from the existing $\kappa+1$ vertices is $1/(\kappa+1)$. The Metropolis sampling-based detailed balanced condition is

$$\frac{P_{k\to k+1}}{P_{k+1\to k}} = -\frac{U\beta N}{\kappa+1}\frac{\prod\limits_\sigma \det D(\kappa+1)}{\prod\limits_\sigma \det D(\kappa)}. \qquad (14)$$

The Metropolis sampling-based acceptance ratio for when a vertex is added is

$$R = \min\left[1, \frac{P_{k\to k+1}}{P_{k+1\to k}}\right].$$

Thus, the calculation of $\det D(\kappa+1)/\det D(\kappa)$ is important. When a vertex is added to $\kappa[(k \to k+1)]$, $\det D(\kappa+1)/\det D(\kappa)$ is calculated efficiently as

$$\begin{aligned}
\frac{\det D(\kappa+1)}{\det D(\kappa)} &= \det[D(\kappa+1)M(\kappa)] = \det\{I + [D(\kappa+1) - D(\kappa)]M(\kappa)\} \\
&= \det\begin{pmatrix} 1 & 0 & \cdots & \mathcal{G}^0(1,\kappa+1) \\ 0 & 1 & \cdots & \mathcal{G}^0(2,\kappa+1) \\ 0 & 0 & \cdots & \mathcal{G}^0(3,\kappa+1) \\ \vdots & \vdots & \vdots & \vdots \\ \sum\limits_i \mathcal{G}^0(\kappa+1,i)M(\kappa)_{i,1} & \sum\limits_i \mathcal{G}^0(\kappa+1,i)M(\kappa)_{i,2} & \cdots & \mathcal{G}^0(\kappa+1,\kappa+1) \end{pmatrix}, \\
\frac{\det D(\kappa+1)}{\det D(\kappa)} &= \det\begin{pmatrix} A & D \\ C & B \end{pmatrix}, \qquad (15)
\end{aligned}$$

where the matrix is composed of four bulk matrices: A is a unit matrix, B is a matrix element $(\kappa+1,\kappa+1)$, C is a row matrix with κ elements, and D is a column matrix with κ elements. Therefore,

$$\begin{aligned}
\frac{\det D(\kappa+1)}{\det D(\kappa)} &= \det\begin{pmatrix} A & D \\ C & B \end{pmatrix} \\
&= \det A \cdot \det(B - CA^{-1}D) \\
&= \mathcal{G}^0(\kappa+1,\kappa+1) \\
&\quad - \sum_{ij}\mathcal{G}_\sigma^0(\kappa+1,i)M_\sigma(\kappa)_{i,j}\mathcal{G}_\sigma^0(j,\kappa+1). \qquad (16)
\end{aligned}$$

Then, Eq. (14) becomes

$$\begin{aligned}
\frac{P_{k\to k+1}}{P_{k+1\to k}} = -\frac{U\beta N}{\kappa+1}\prod_\sigma\Big[&\mathcal{G}^0(\kappa+1,\kappa+1) \\
&- \sum_{ij}\mathcal{G}_\sigma^0(\kappa+1,i)M_\sigma(\kappa)_{i,j}\mathcal{G}_\sigma^0(j,\kappa+1)\Big].
\end{aligned}$$

The unknown in the above equation is the matrix $M_\sigma(\kappa)$. The relationship between $M_\sigma(\kappa)$ and $M_\sigma(\kappa+1)$ is obtained from Eq. (17):

$$M_\sigma(\kappa+1) = \det\begin{pmatrix} \cdot & \cdot & \cdot & -\lambda^{-1}L_{1,\kappa+1} \\ \cdot & M'_\sigma & \cdot & -\lambda^{-1}L_{2,\kappa+1} \\ \cdot & \cdot & \cdot & -\lambda^{-1}L_{3,\kappa+1} \\ \vdots & \vdots & \vdots & \vdots \\ -\lambda^{-1}R_{\kappa+1,1} & -\lambda^{-1}R_{\kappa+1,2} & \cdots & -\lambda^{-1} \end{pmatrix}, \tag{17}$$

where the matrix elements are defined as

$$M'_{\sigma ij} = M(\kappa)_{ij} + L_{i,\kappa+1}\lambda^{-1}R_{\kappa+1,j},$$

$$R_{ij} = \sum_n \mathcal{G}^0_\sigma(i,n)M(\kappa)_{nj},$$

$$L_{ij} = \sum_n M(\kappa)_{in}\mathcal{G}^0_\sigma(n,j),$$

$$\lambda = \frac{\det D(\kappa+1)}{\det D(\kappa)}.$$

2) When the lattice model has N sites and a vertex is subtracted ($\kappa \to \kappa-1$), the Metropolis sampling-based detailed balanced condition is

$$\frac{P_{k\to k-1}}{P_{k-1\to k}} = -\frac{U\beta N}{\kappa+1}\frac{\prod_\sigma \det D(\kappa-1)}{\prod_\sigma \det D(\kappa)}.$$

Next, we calculate the physical quantity. For spin-up, the system's single-particle Green's function is

$$\begin{aligned} G_\uparrow(\tau)_{ij} &= -\left\langle T_\tau c_\uparrow(i)c^\dagger_\uparrow(j)\right\rangle = -\frac{1}{\mathcal{Z}}\mathrm{tr}\left(T_\tau c_\uparrow(i)c^\dagger_\uparrow(j)\mathrm{e}^{-\beta H}\right) \\ &= -\frac{1}{\mathcal{Z}}\mathrm{tr}\left(T_\tau c_\uparrow(i)c^\dagger_\uparrow(j)\exp(-\beta H_0)T\tau\exp[\int_\beta^0 U\sum_i n_{i\uparrow}(\tau)n_{i\downarrow}(\tau)\mathrm{d}\tau]\right) \\ &= -\frac{1}{\mathcal{Z}}\mathrm{tr}\left[T_\tau c_\uparrow(i)c^\dagger_\uparrow(j)\exp(-\beta H_0)\sum_\kappa\frac{(-U)^\kappa}{\kappa!}\int\mathrm{d}1\cdots\int\mathrm{d}\kappa T_\tau n_{i\uparrow}(1)\cdots n_{i\uparrow}(\kappa)T_\tau n_{i\downarrow}(1)\cdots n_{i\downarrow}(\kappa)\right] \\ &= -\frac{\mathcal{Z}_0}{\mathcal{Z}}\sum_\kappa\frac{(-U)^\kappa}{\kappa!}\int\mathrm{d}1\cdots\int\mathrm{d}\kappa\left\langle T_\tau c_\uparrow(i)c^\dagger_\uparrow(j)n_{i\uparrow}(1)\cdots n_{i\uparrow}(\kappa)\right\rangle_0\left\langle T_\tau n_{i\downarrow}(1)\cdots n_{i\downarrow}(\kappa)\right\rangle_0, \end{aligned} \tag{18}$$

and $\langle T_\tau c_\uparrow(i)c^\dagger_\uparrow(j)n_{i\uparrow}(1)\cdots n_{i\uparrow}(\kappa)\rangle_0 = \det D(\kappa+1)$.

$$\begin{aligned} G_\uparrow(\tau)_{ij} &= \frac{\displaystyle\sum_\kappa\frac{(-U)^\kappa}{\kappa!}\int\mathrm{d}1\cdots\int\mathrm{d}\kappa\det[D_\uparrow(\kappa+1)D_\downarrow(\kappa)]}{\displaystyle\sum_\kappa\frac{(-U)^\kappa}{\kappa!}\int\mathrm{d}1\cdots\int\mathrm{d}\kappa\det[D_\uparrow(\kappa)D_\downarrow(\kappa)]} \\ &= \frac{\displaystyle\sum_\kappa\frac{(-U)^\kappa}{\kappa!}\int\mathrm{d}1\cdots\int\mathrm{d}\kappa\det[D_\uparrow(\kappa)D_\downarrow(\kappa)]\frac{\det[D_\uparrow(\kappa+1)D_\downarrow(\kappa)]}{\det[D_\uparrow(\kappa)D_\downarrow(\kappa)]}}{\displaystyle\sum_\kappa\frac{(-U)^\kappa}{\kappa!}\int\mathrm{d}1\cdots\int\mathrm{d}\kappa\det[D_\uparrow(\kappa)D_\downarrow(\kappa)]}, \end{aligned} \tag{19}$$

where

$$\frac{\det[D_\uparrow(\kappa+1)D_\downarrow(\kappa)]}{\det[D_\uparrow(\kappa)D_\downarrow(\kappa)]}$$

is the measurement function and

$$D_\uparrow(\kappa+1) = \begin{pmatrix} \mathcal{G}^0_\uparrow(1,1) & \mathcal{G}^0_\uparrow(1,2) & \cdots & \mathcal{G}^0_\uparrow(1,\kappa) & \mathcal{G}^0_\uparrow(1,j) \\ \mathcal{G}^0_\uparrow(2,1) & \mathcal{G}^0_\uparrow(2,2) & \cdots & \mathcal{G}^0_\uparrow(2,\kappa) & \mathcal{G}^0_\uparrow(2,j) \\ \vdots & \vdots & \vdots & \vdots & \vdots \\ \mathcal{G}^0_\uparrow(\kappa,1) & \mathcal{G}^0_\uparrow(\kappa,2) & \cdots & \mathcal{G}^0_\uparrow(\kappa,\kappa) & \mathcal{G}^0_\uparrow(\kappa,j) \\ \mathcal{G}^0_\uparrow(i,1) & \mathcal{G}^0_\uparrow(i,2) & \cdots & \mathcal{G}^0_\uparrow(i,\kappa) & \mathcal{G}^0_\uparrow(i,j) \end{pmatrix}.$$

Thus,

$$\begin{aligned} G_\uparrow(\tau)_{ij} &= \frac{\det[D_\uparrow(\kappa+1)D_\downarrow(\kappa)]}{\det[D_\uparrow(\kappa)D_\downarrow(\kappa)]} \\ &= \mathcal{G}^0_\uparrow(i,j) - \sum_{pq}\mathcal{G}^0_\uparrow(i,p)M(\kappa)_{p,q}\mathcal{G}^0_\uparrow(q,j). \end{aligned} \tag{20}$$

3 Results

In this article, we review our CDMFT-based investigation on the quantum phase transitions in two-dimensional lattices, including the TKL, the decorated

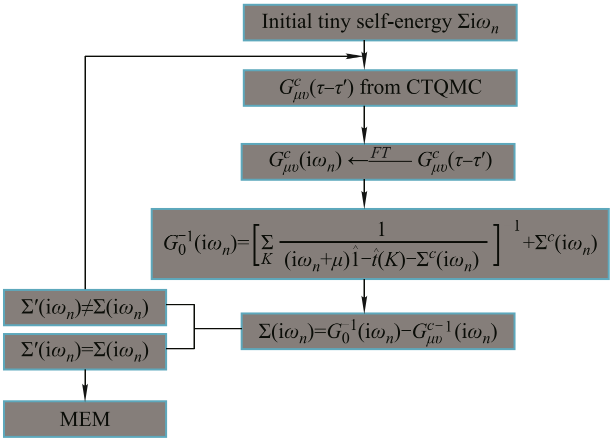

Fig. 3 Sketch map for the combination of cellular dynamical mean-field theory (CDMFT) and continuous-time quantum Monte Carlo (CTQMC) algorithm.

honeycomb lattice, the Shastry–Sutherl and lattice, and the square–octagon lattice.

The TKL, as seen in Fig. 4(a), is a two-dimensional geometrically frustrated lattice that is found in the new material $Cu_9X_2(cpa)_2 \cdot xH_2O$, (where cpais2-carboxypentonic acid, a derivative of ascorbic acid, and X = F, Cl, Br), in which the Cu spins form the geometrically frustrated TKL. This lattice is also realized by cold atoms in an optical lattice. In contrast with other frustrated systems such as the triangular lattice and the Kagomé lattice, the "triangles-in-triangles" structure on the TKL induces two different sublattices.

The decorated honeycomb lattice in Fig. 5(a), also called the star lattice, is a "cousin" of both the honeycomb lattice and the Kagomé lattice because it interpolates between the two. If the triangles at the vertices of the underlying honeycomb lattice shrink to their center points, a honeycomb lattice is recovered while expanding the triangles until their corners touch to produce a Kagomé lattice. The decorated honeycomb lattice has been found in new polymeric iron (III) acetate.

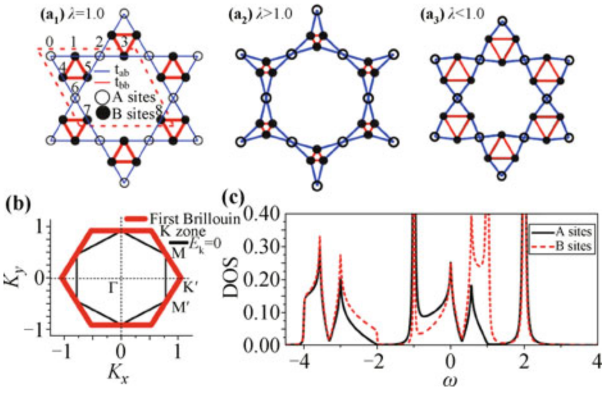

Fig. 4 **(a$_1$)** Symmetric TKL with $\lambda = 1$. The blue lines represent the hopping between A sites and B sites. The red lines denote the hopping between B sites. **(a$_2$)** TKL is similar to the Kagomé lattice with $\lambda > 1$. **(a$_3$)** TKL is similar a system composed of many triangular plaquettes with $\lambda < 1$. **(b)** The red lines indicate the first Brillouin zone of the TKL and the black lines correspond to the Fermi surface for the noninteracting case. The Γ, K, M, K′, M′ points denote the points in the first Brillouin zone with different symmetry. **(c)** Density of states of the symmetric TKL for A sites and B sites when U=0 at half filling. Reproduced from Ref. [26].

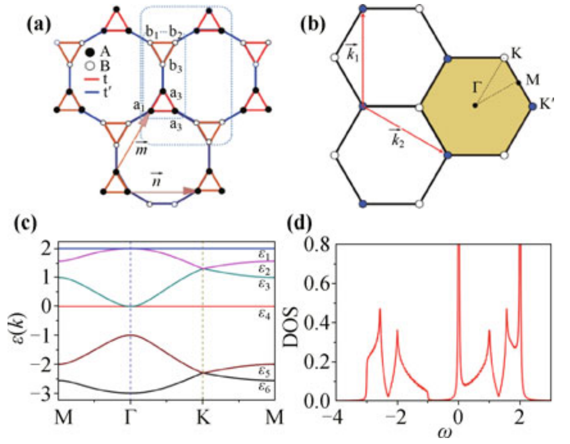

Fig. 5 **(a)** Sketch map of decorated honeycomb lattice. Solid circles denote A sites and open circles mean B sites. The cluster contains six sites: a_1, a_2, a_3, b_1, b_2, and b_3. Inside the small rectangular area (*dotted blue line*) and large rectangular area (*dotted blue line*) are the 6- and 12-site clusters, respectively, used in our analysis. Arrows m and n are the real lattice vectors. **(b)** K-space vectors k_1 and k_2 and first Brillouin zone (*shaded yellow hexagon*) of the decorated honeycomb lattice. **(c)** Band structure of the tight-binding model along the path M-Γ-K-M shown in (b), in which $\varepsilon_1, \varepsilon_2, \varepsilon_3, \varepsilon_4, \varepsilon_5$, and ε_6 represent six energy bands for tight-binding approximation. There are Dirac points at K and K′(not shown) and the quadratic band crossing point at Γ. **(d)** Noninteracting density of states (DOS) of the system at half-filling $f = 1/2$. There are four van Hove singularities and two δ peaks. Reproduced from Ref. [43].

The two-dimensional lattice in Fig. 6(a), filled with Cu^{2+} ions, is topologically equivalent to the Shastry–Sutherl and lattice in Fig. 6(b) and was found in $SrCu_2(BO_3)_2$.

The square–octagon lattice is a bipartite lattice that is viewed as a square lattice in which each vertex is decorated with a tilted square, as seen in Fig. 7(a). The quasi-square–octagon lattice was found in the $(10\bar{1}0)$ surface of the functional material ZnO by first-principle calculations and aberration-corrected transmission electron microscopy (ACTEM) experimental observations during its pressure-induced phase transition.

We adopted the popular Hubbard model to describe the behavior of strongly correlated fermions in the two-dimensional lattices discussed above. The Hamiltonians for the different lattices are different and are respectively as follows:

For the TKL,

$$H = -\sum_{\langle i,j\rangle\sigma} t_{ij} c^{\dagger}_{i\sigma} c_{j\sigma} + U\sum_{i} n_{i\uparrow} n_{i\downarrow} + \mu\sum_{i\sigma} n_{i\sigma}, \qquad (21)$$

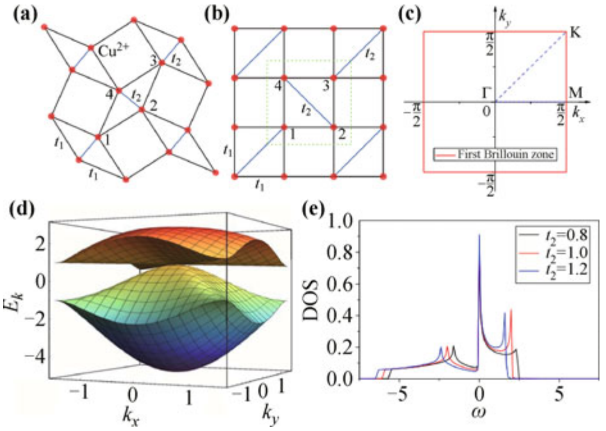

Fig. 6 **(a)** Arrangement of Cu^{2+} ion in SrCu$_2$(BO$_3$)$_2$. **(b)** Sketch map of Shastry-Sutherland lattice which topologically equivalent to (a). The dashed green line marks the four-site cluster which contains four atoms labeled by 1, 2, 3, and 4. t_1 and t_2 are the nearest-neighbor hopping energy and the diagonal hopping energy respectively. We set the distance between the nearest neighbors as the length unit and $t_1 = 1.0$ as the energy unit. **(c)** First Brillouin zone of Shastry–Sutherland lattice. Γ, K, and M denote high symmetry points. **(d)** Tight-binding dispersion for $t_2 = 1.0$; **(e)** Density of states at half-filling for $t_2 = 0.8$, 1.0, and 1.2, respectively while $U = 0$. Reproduced from Ref. [31].

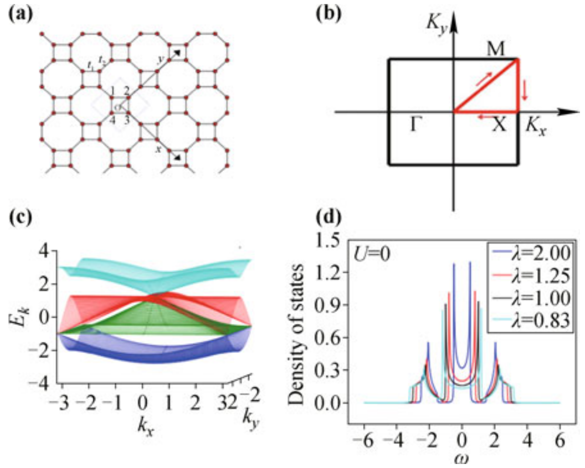

Fig. 7 **(a)** Sketch map of square-octagon lattice and illustration of hopping term t_1 and t_2, where t_1 and t_2 represent hopping factors between the nearest-neighboring sites in the same square and between the endpoints of the different squares' linking line, respectively. **(b)** Reduced Brillouin zone of square-octagon lattice. **(c)** Energy band in the reduced Brillouin zone of square-octagon lattice. **(d)** Density of states of the square-octagon lattice without interaction for different anisotropic parameter. Reproduced from Ref. [32].

where t_{ij} is the nearest-neighbor hopping energy, U is the Coulomb interaction, μ is the chemical potential, $c^\dagger_{i\sigma}$ and $c_{j\sigma}$ denote the creation and annihilation operators, respectively, and $n_{i\sigma} = c^\dagger_{i\sigma}c_{i\sigma}$ is the particle number density operator. We also introduced the parameterλ, a asymmetry factor defined as $\lambda = t_{ab}/t_{bb}$ and which can be adjusted by suppressing samples in experiments. For convenience, we set $t_{bb} = 1.0$ as the energy unit.

For the decorated honeycomb lattice, we considered two-component fermions trapped in the lattice with nearest-neighbor hopping t on vertex triangles and $t'(t' = \lambda t)$ between triangles as shown in Fig. 5(a); $t = 1$ was defined as the energy scale.

$$H = -t\sum_{\langle ij\rangle\sigma\Delta} c^\dagger_{i\sigma}c_{j\sigma} - t'\sum_{\langle ij\rangle\sigma\Delta\to\Delta} c^\dagger_{i\sigma}c_{j\sigma} - \mu\sum_{i\sigma} n_{i\sigma} + U\sum_i n_{i\uparrow}n_{i\downarrow}, \tag{22}$$

where $c^\dagger_{i\sigma}$ and $c_{j\sigma}$ are the creation and the annihilation operators offer m ions with spin σ on sites i and j, respectively, $n_{i\sigma} = c^\dagger_{i\sigma}c_{i\sigma}$ is the density operator represents the vertex triangle, U is the on-site repulsion interaction, and μ is the chemical potential. The Hamiltonian of the decorated honeycomb lattice satisfies $SU(2)$ spin symmetry, time-reversal symmetry, and C6 lattice rotational symmetry.

For the Shastry–Sutherl and lattice, the Hamiltonian is defined as

$$H = -t_1\sum_{\langle ij\rangle_1,\sigma} c^\dagger_{i\sigma}c_{j\sigma} - t_2\sum_{\langle ij\rangle_2,\sigma} c^\dagger_{i\sigma}c_{j\sigma} + U\sum_i n_{i\uparrow}n_{i\downarrow}, \tag{23}$$

where $c^\dagger_{i\sigma}$ and $c_{j\sigma}$ are the creation and annihilation operators of fermions with spin σ on sites i and j, respectively, $n_{i\sigma} = c^\dagger_{i\sigma}c_{i\sigma}$ is the density operator, and σ is the spin index, the value of which is up or down.

For the square–octagon lattice, the Hamiltonian is

$$H = -t_1\sum_{i,j\in,\sigma} c^\dagger_{i\sigma}c_{j\sigma} - t_2\sum_{\to,\sigma} c^\dagger_{i\sigma}c_{j\sigma} + U\sum_i n_{i\uparrow}n_{i\downarrow} - \mu\sum_{i,\sigma} n_{i\sigma} + h.c. \tag{24}$$

where $c^\dagger_{i\sigma}$ and $c_{j\sigma}$ are the creation and annihilation operators of fermions with spin σ on sites i and j, respectively, $n_{i\sigma} = c^\dagger_{i\sigma}c_{i\sigma}$ is the density operator, μ is the chemical potential, and σ is the spin index, the value of which is up or down. The first two terms in this Hamiltonian account for the kinetic energy of the system, which is characterized by the coefficient factors t_1 and t_2, where t_1 is the hopping between the nearest-neighbor sites in the same square lattice and t_2 is the hopping between the endpoints of the line that links the two nearest-neighbor square lattices. The third term describes the on-site repulsive interaction ($U > 0$) between fermions with opposite spin. Here, we set t_1 as the energy unit ($t_1 = 1$). Finally, to reach the half-filled case, μ should equal zero for this lattice system. In addition, we define an anisotropic parameter λ such that $\lambda = t_1/t_2$.

At $U = 0$, the Hubbard model translates into a tight-binding approximation. The density of states and the energy dispersion in the reduced Brillouin zone for the two-dimensional lattices discussed above at $U = 0$ are presented below. As an example, we use the square–octagon lattice with fermions to explain the process of obtaining the density of states and the energy dispersion in the reduced Brillouin zone. For $U = 0$ and $\mu = 0$, the Hubbard model translates into a tight-binding approximation Hamiltonian. Thus, the Hamiltonian in momentum space is $H_0 = \sum_k \Psi_k^{\dagger}\mathcal{H}_k^0\Psi_k$, in which $\Psi_k = (c_{1k\uparrow}, c_{2k\uparrow}, c_{3k\uparrow}, c_{4k\uparrow}, c_{1k\downarrow}, c_{2k\downarrow}, c_{3k\downarrow}, c_{4k\downarrow})^{\mathrm{T}}$. The creation and annihilation operators in each unit cell are the four sites where the index $i = 1,\ 2,\ 3,\ 4$, as illustrated in Fig. 7(a). k is the location in the first Brillouin zone and ↑ and ↓ indicate spin-up and spin-down. Because $\mathcal{H}_k^0$ is decoupled in spin states, i.e., $\mathcal{H}_k^0$ is block diagonalized, it takes the following form:

$$\mathcal{H}_k^0 = -\begin{pmatrix} 1 & 0 \\ 0 & 1 \end{pmatrix} \otimes \begin{pmatrix} 0 & t_1\mathrm{e}^{\mathrm{i}k_x+\mathrm{i}k_y} & 2t_2\mathrm{e}^{-\mathrm{i}\sqrt{2}k_y} & t_1\mathrm{e}^{-\mathrm{i}k_x+\mathrm{i}k_y} \\ t_1\mathrm{e}^{-\mathrm{i}k_x-\mathrm{i}k_y} & 0 & t_1\mathrm{e}^{-\mathrm{i}k_x+\mathrm{i}k_y} & 2t_2\mathrm{e}^{-\mathrm{i}\sqrt{2}k_x} \\ 2t_2\mathrm{e}^{\mathrm{i}\sqrt{2}k_y} & t_1\mathrm{e}^{\mathrm{i}k_x-\mathrm{i}k_y} & 0 & t_1\mathrm{e}^{-\mathrm{i}k_x-\mathrm{i}k_y} \\ t_1\mathrm{e}^{\mathrm{i}k_x-\mathrm{i}k_y} & 2t_2\mathrm{e}^{-\mathrm{i}\sqrt{2}k_x} & t_1\mathrm{e}^{\mathrm{i}k_x+\mathrm{i}k_y} & 0 \end{pmatrix}. \tag{25}$$

The energy band and the energy dispersion in the first Brillouin zone of the square–octagon lattice within the framework of a tight-binding approximation are obtained by diagonalizing $\mathcal{H}_k^0$ and are shown in Figs. 7(c) and 8, respectively. The density of states of the square–octagon lattice without interaction is presented in Fig. 7(d).

The energy dispersion and density of states of the decorated honeycomb lattice and the Shastry–Sutherl and lattice without interaction are shown in Figs. 5(c) and 9 and Figs. 5(d) and 6(d), respectively.

To investigate the transition between metal and insulator in these two-dimensional lattices, half-filled with fermions for finite on-site repulsive interaction, we have to calculate the density of states (or the momentum-resolved spectrum), double occupancy, and the evolution of the Fermi surface of these systems.

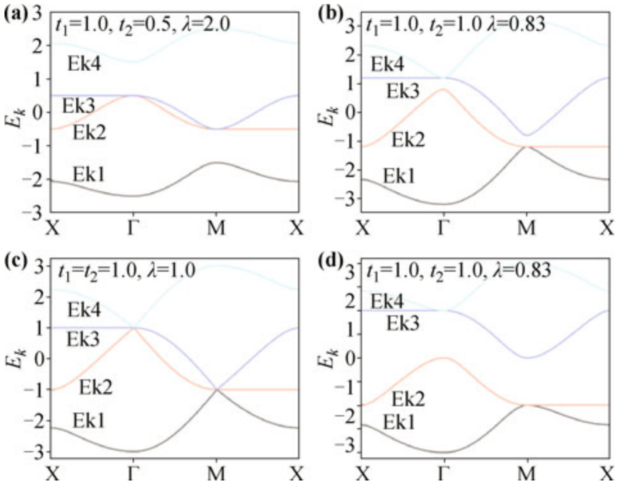

Fig. 8 Energy dispersion of isotropic square-octagon lattice along the line between high symmetric points in the reduced Brillouin zone. **(a)** Energy band E_{k2} and E_{k3} contact at Γ point and M point for $\lambda = 2.0$ and the system is in metallic state. **(b)** Energy band E_{k2}, E_{k3} and E_{k4} cross at Γ point while E_{k1}, E_{k2} and E_{k3} cross at M point for $\lambda = 1.0$. **(c)** The band E_{k1} and E_{k2} contact at M point while the band E_{k3} and E_{k4} contact at Γ point for $\lambda = 0.83$ and the system is in metallic states. **(d)** Band E_{k2} and band E_{k3} are completely separated by Fermi energy level and the system turns into insulating states. t_1 fixed for all case and equals 1. Reproduced from Ref. [32].

The momentum-resolved spectrum $A_k(\omega)$ of a TKL is calculated using the maximum entropy method; the results are shown in Fig. 10. Figure 10(b) shows that with an increase in interaction, a visible gap near the Fermi energy appears which indicates an insulating state. The $A_k(\omega)$ of the plaquette insulator is shown in Fig. 10(c), and Fig. 10(d) shows there is visible gap near the Fermi energy when the system stays in the Kondo metal state. The momentum-resolved spectral function is obtained using angle-resolved photoemission spectroscopy (ARPES) experiments and the plaquette insulator. Kondo metal can be found in real samples.

After calculating the self-energy that satisfies the accuracy requirement, we used the maximum entropy method [64] to calculate the density of states of the two-dimensional strongly correlated fermion systems discussed above. The formula for the density of states is

$$D(\omega) = -\frac{1}{\pi}\sum_{i=1}^{N_{\mathrm{c}}}[\mathrm{Im}G_{ii}(\omega - \mathrm{i}\delta)],$$

where the site index and N_c is the number of sites in the cluster. For the TKL, $N_c = 8$, for the decorated honeycomb lattice, $N_c = 6$, and for the Shastry–Sutherl and and square–octagon lattices, $N_c = 4$.

In general, with an increase in the on-site repulsive interaction U, the probability of more than one fermion occupying the same lattice site decreases and eventually only one fermion is confined per lattice site at a certain large value of U. This confinement is described as double occupancy (D_{occ}), an important quantity used to characterize the critical point in Mott phase transitions. D_{occ}

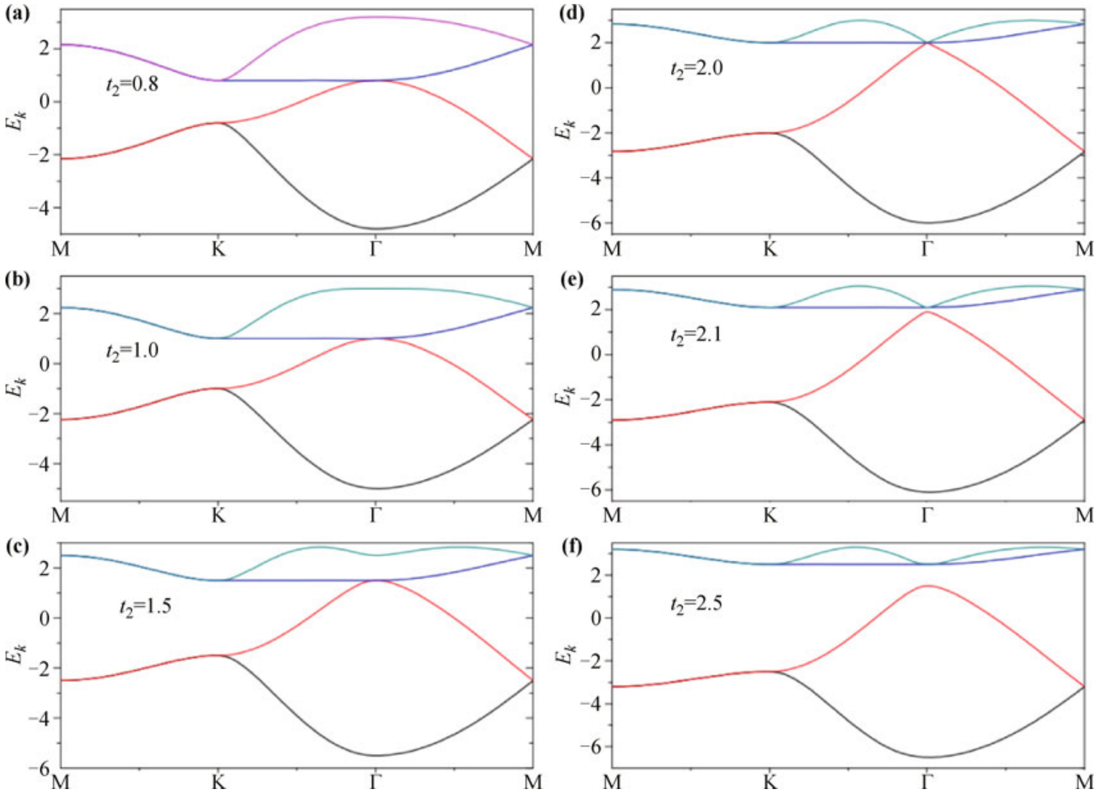

Fig. 9 Energy dispersion of Shastry–Sutherland lattice along the line between high symmetric points in the reduced Brillouin zone. **(a)** $t_2 = 0.8$, **(b)** $t_2 = 1.0$, **(c)** $t_2 = 1.5$, **(d)** $t_2 = 2.0$, **(e)** $t_2 = 2.1$, and **(f)** $t_2 = 2.5$. We label I II III and IV from top to bottom. Band II and III begin to separate when $t_2 = 2.0$ and the system becomes a band insulator at half-filling. We focus on the case when $t_2 < 2.0$ in this report. Reproduced from Ref. [31].

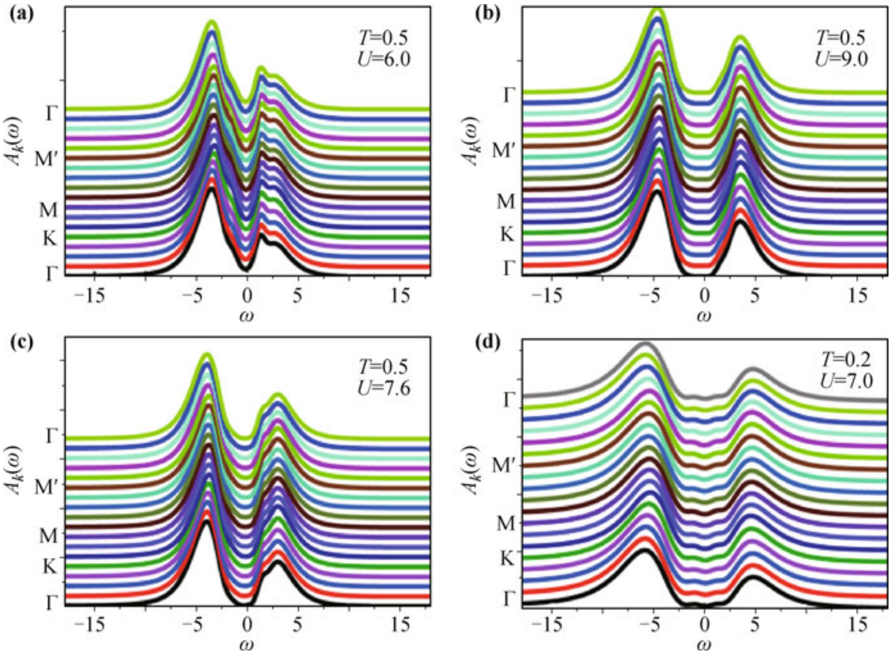

Fig. 10 The momentum resolved spectrum $A_k(\omega)$ at $\lambda = 0.6$. **(a)** The metallic phase at $U = 6$ and $T = 0.5$. **(b)** The Mott insulating phase at $U = 9$ and $T = 0.5$. A clearly visible single particle gap shows up around the Fermi energy. **(c)** The plaquette insulating phase at $U = 7.6$ and $T = 0.5$. A small gap shows up in this phase. **(d)** The Kondo metallic phase at $U = 7$ and $T = 0.2$, in which A sites are metallic and B sites are insulating. The single particle gap vanishes in this phase. Reproduced from Ref. [28].

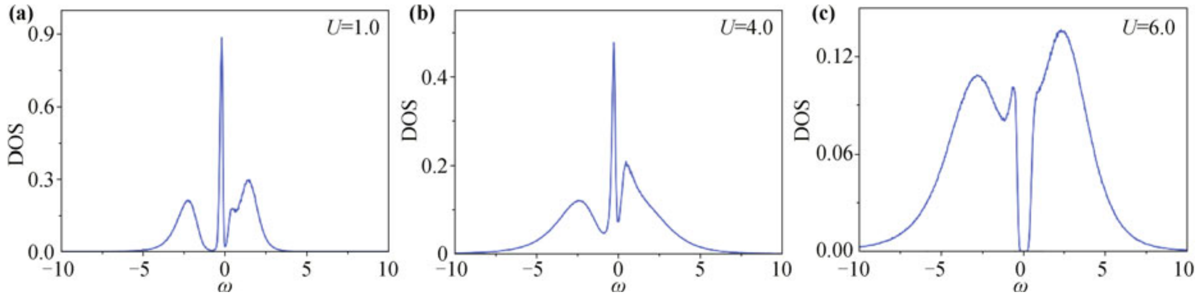

Fig. 11 The density of states of the decorated honeycomb lattice for finite interaction at $T = 0.05$. **(a)** The zero density in the Fermi level at $U = 1.0$ shows that the system is a semimetal. **(b)** A finite density at the Fermi level for $U = 4.0$, which indicates that the system stays in the Nematic metal phase. **(c)** A charge gap is opened at $U = 6.0$ means that the system is an insulator. Reproduced from Ref. [43].

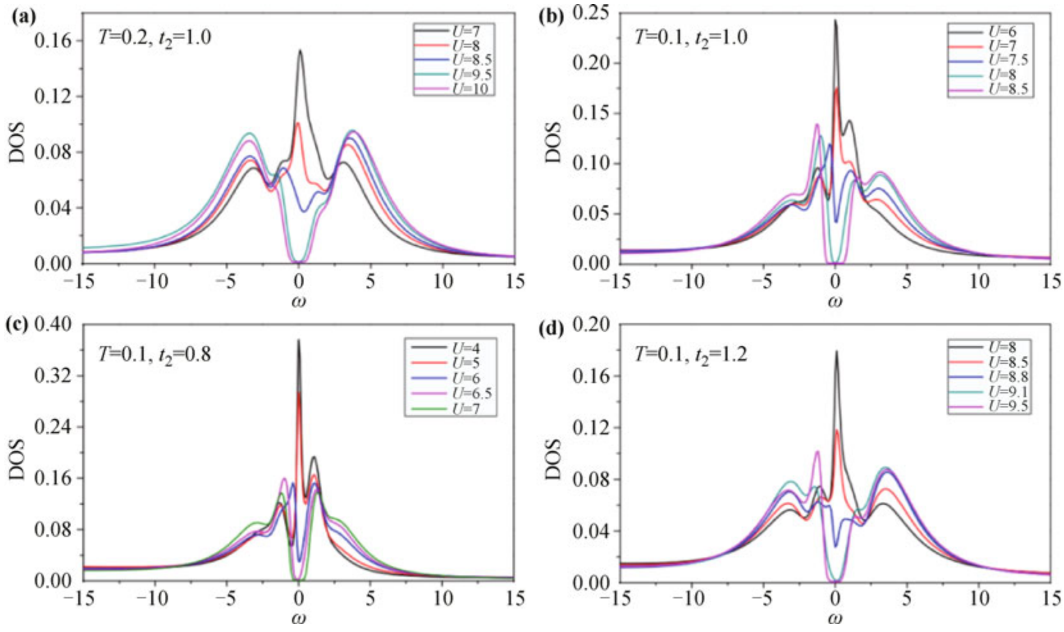

Fig. 12 The density of states of the Shastry–Suther land lattice for finite interaction. **(a)** Density of state (DOS) for different on-site repulsive interaction U at $T = 0.2$ and $t_2 = 1.0$. Mott metal-insulator transition happens at $U = 9.5$, in which an obvious energy gap appears around the Fermi level. Density of states for **(b)** $T = 0.1$, $t_2 = 1.0$; **(c)** $T = 0.1$, $t_2 = 0.8$ and **(d)** $T = 0.1$, $t_2 = 1.2$ are also plotted, where the transition points are $U = 8$, 6.5, and 9.1, respectively. Reproduced from Ref. [31].

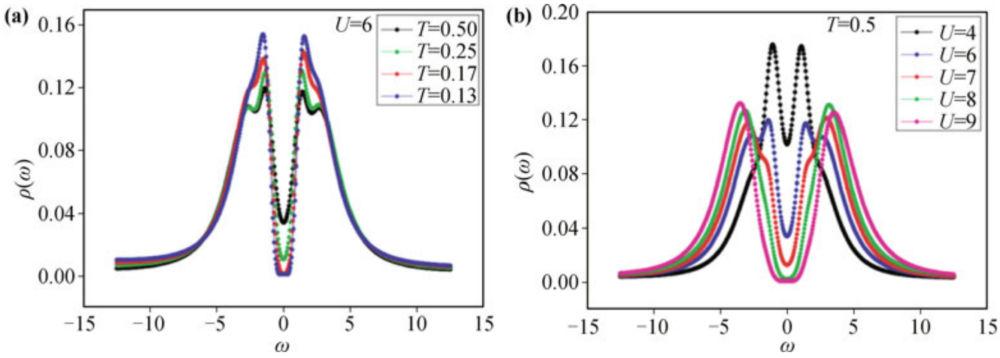

Fig. 13 The density of states of the isotropic square-octagon lattice for finite interaction. **(a)** The density of states for the different temperature while the on-site repulsive interaction fixed at $U/t_1 = 6$. The critical temperature for Mott transition is $T/t_1 = 0.17$. **(b)** The density of states for different on-site repulsive interaction while the temperature fixed $T/t_1 = 0.5$, the critical on-site repulsive interaction is $U/t_1 = 8$. Reproduced from Ref. [32].

indicates the transition order and is used to describe the localization of the electrons in strongly correlated electron systems. The formula for double occupancy is

$$D_{\mathrm{occ}} = \partial F/\partial U = \frac{1}{N_{\mathrm{c}}}\sum_{i=1}^{N_{\mathrm{c}}}\langle n_{i\uparrow}n_{i\downarrow}\rangle,$$

where F is free energy, U is the on-site repulsive interaction, and N_c is the number of sites in one cluster. The arrows in Figs. 14–17, which show the double occupancy of different lattices, indicate the phase transition point at different temperatures. The smooth continuity of the evolution of double occupancy is characteristic of a second-order Mott transition that occurs with an increase in the on-site repulsive interaction U, while discontinuity signals a first-order phase transition, such as that near the critical point $U_{\mathrm{NM-AFI}}$ in the decorated honeycomb lattice. We conclude that D_{occ} decreases as the interaction increases because the itinerancy of the atoms is suppressed. The double occupancies for TKL, decorated honeycomb lattice, Shastry–Sutherland lattice, and square–octagon lattice are shown in Figs. 14–17, respectively. We conclude from these figures that with an increase in the on-site repulsive interaction, the double occupancy trends toward zero, which indicates the appearance of the Mott insulating state from a different perspective. When the interaction is stronger than the critical interaction of the Mott transition, the effect of temperature on D_{occ} is weakened and D_{occ} for different temperatures consistently trends toward zero, which shows that the temperature does not distinctly affect double occupancy.

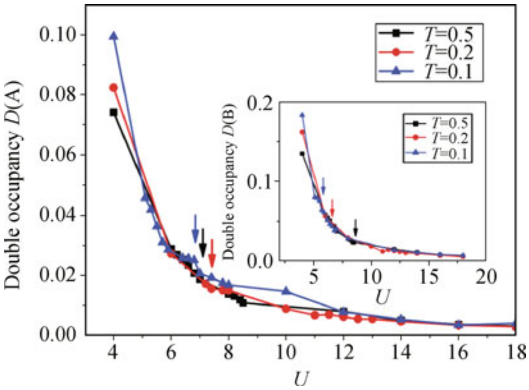

Fig. 14 Thedouble occupancy on the A sites as a function of on-site repulsive interaction U for different temperatures T at $\lambda = 0.6$. The inset figure shows the double occupancy on the B sites. The arrows with different colors show the phase transition points at different temperatures T. Reproduced from Ref. [28].

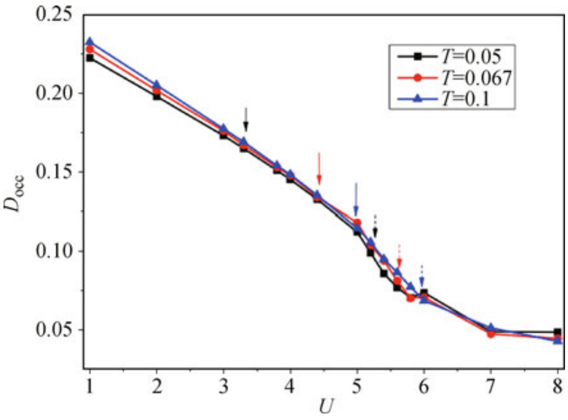

Fig. 15 Thedouble occupancy (D_{occ}) of the decorated honeycomb lattice and the on-site repulsive interaction U for various temperatures T. Solid arrows indicates the critical points of SM-NM crossover while dashed arrows show the critical points of the NM-AFM insulating phase transition. Reproduced from Ref. [43].

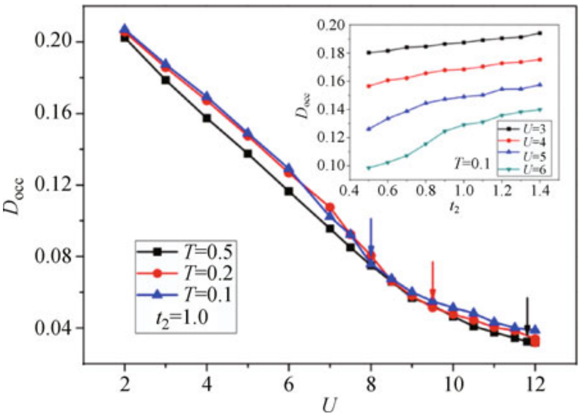

Fig. 16 The double occupancy (D_{occ}) of the Shastry–Sutherland lattice as function of the on-site repulsive interaction U for $T = 0.1$, 0.2and 0.5 when $t_2 = 1.0$. The blue, red, and black arrows mark the critical U's of Mott transition for $T = 0.1$, 0.2 and 0.5, and the values are 8, 9.5, and 11.8 respectively. Inset: The evolution of Docc as a function of t_2 for different on-site repulsive interaction at $T = 0.1$. Reproduced from Ref. [31].

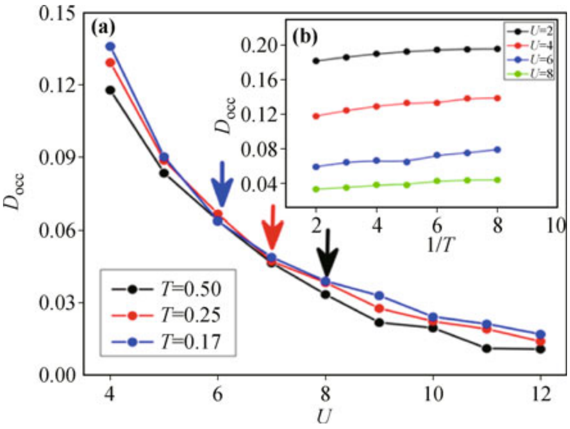

Fig. 17 The double occupancy (D_{occ}) of the square-octagon lattice as function of the on-site repulsive interaction U for $T = 0.17$, 0.25, and 0.5. **(a)** The evolution of the double occupancy as a function of on-site repulsive interaction U for different temperature T. The arrows hint the corresponding value of Mott transition for different temperature. **(b)** The value of the double occupancy under certain temperature for different on-site repulsive interaction U. Reproduced from Ref. [32].

The spectral function of the Fermi surface,

$$A(k;\omega=0)\approx -\frac{1}{\pi}\lim_{\omega\to 0}\mathrm{Im}G_k(k,\mathrm{i}\omega_n)$$

reveals the evolution of the metal–insulator properties of the two-dimensional lattices half-filled with fermions. $G_k(\omega)$ is a k-dependent Green's function, where k is the wave vector in the original Brillouin zone.

The spectral function of the TKL on a Fermi surface for different U, T, and λ is presented in Fig. 18. Figure 18(b$_1$) shows that there are six peaks near the M point in Fig. 4(b) for $\lambda = 1$. The Fermi surface shrinks with an increase in the on-site repulsive interaction U because of the localization of electrons. Figure 18(a$_1$) shows that the Fermi surface at $\lambda = 0.6$ is similar to a system composed of many triangular plaquettes. The Fermi surface at $\lambda = 1.25$ is similar to a Kagomé lattice [see Fig. 18(c$_1$)]. As the on-site repulsive interaction U increases, the Fermi surface develops into a fiat plane that shows the localization of electrons, as shown in Figs. 18(a$_2$)–(c$_2$). The spectral function can be measured using ARPES experiments.

The distribution of the spectral weight $A(k,\omega)$ of the Shastry–Sutherl and lattice at zero frequency ($\omega = 0$) and $T = 0.1$ for different U and t_2 are presented in Fig. 19. The location of the maximum of $A(k,\omega = 0)$ is seen as the Fermi surface. Figure 19 shows that when U is small, the spectral function has sharp peaks at the center and along the two intersecting diagonals of the first Brillouin zone, which is weakly renormalized, compared to the noninteraction case, and exhibits a well-defined Fermi surface. With increasing interaction, the peaks decrease and finally vanish when there is a Mott transition due to the localization of particles. Decreasing frustration also makes the Fermi surface shrink.

The first two Matsubara frequencies are linearly extrapolated to estimate the self-energy at zero frequency. The Fermi surface of the isotropic square–octagon lattice, half-filled with fermions, for different interactions U/t_1 at a fixed temperature $T/t_1 = 0.1$ is shown in Figs. 20(a$_2$), (b$_2$), and (c$_2$). In addition, Fig. 20 shows the Fermi surface of the anisotropic square–octagon lattice for $U/t_1 = 4$, 6, 8, while $T/t_1 = 0.1$. With the decrease of λ for a fixed U, the amplitude of the spectral weight increases because of the localization of particles.

We discuss the magnetic properties of each state in every two-dimensional lattice with fermions by defining magnetic order parameters. For the TKL, we define the ferrimagnetic order parameter $m = (1/N)\sum_i \mathrm{sgn}(i)(\langle n_{i\uparrow}\rangle - \langle n_{i\downarrow}\rangle)$, where i denotes the sites in the cluster shown in Fig. 4(a$_1$) and N is the number of sites in the cluster. The sign function $\mathrm{sgn}(i) = 1$ when $i = 0$, 2, 6 and $\mathrm{sgn}(i) = -1$ when $i = 1$, 3, 4, 5, 7, 8. The single-particle energy gap ΔE and m, a function of the on-site repulsive interaction U, for $\lambda = 1$ and $T = 0.2$ are shown in Fig. 21. The Mott transition points of the A and B sites coexist when asymmetry is absent. A single particle's energy gap opens when $U = 8.5$. The ferromagnetic order parameter $m = 0$ for $U < U_c = 13.8$, which indicates that the system is in a paramagnetic insulating state. This nonmagnetic state with a visible energy gap is similar to the short-range resonating-valence-bond state (RVB) found in other systems, such as the honeycomb lattice. We argue that this paramagnetic insulating state is a candidate for short-range RVB spin liquid because of the absence of any long-range correlations. There

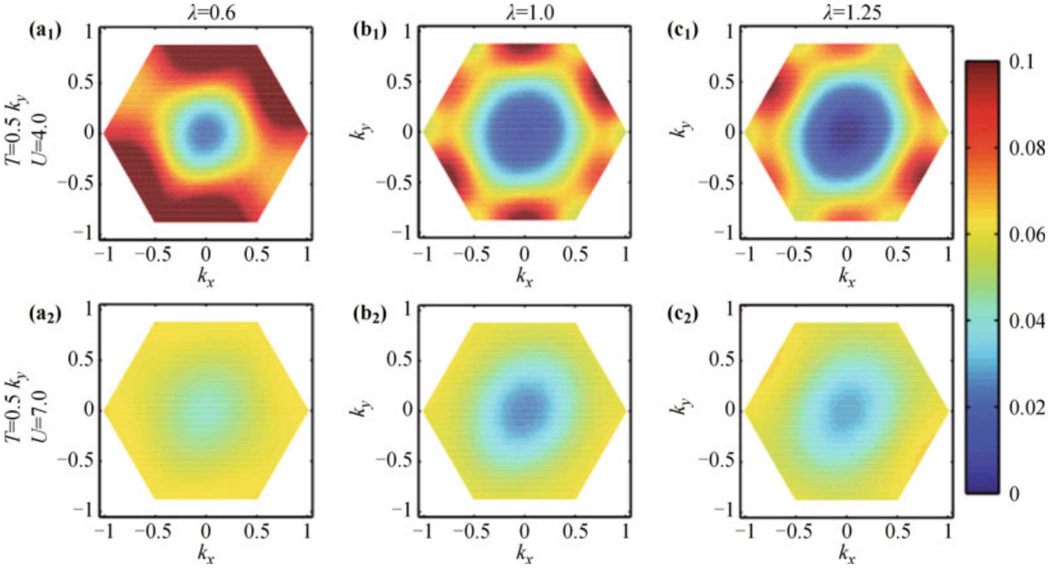

Fig. 18 The evolution of the spectral function on Fermi surface. **(a)** $\lambda = 0.6$, **(b)** $\lambda = 1.0$, **(c)** $\lambda = 1.25$. Reproduced from Ref. [28].

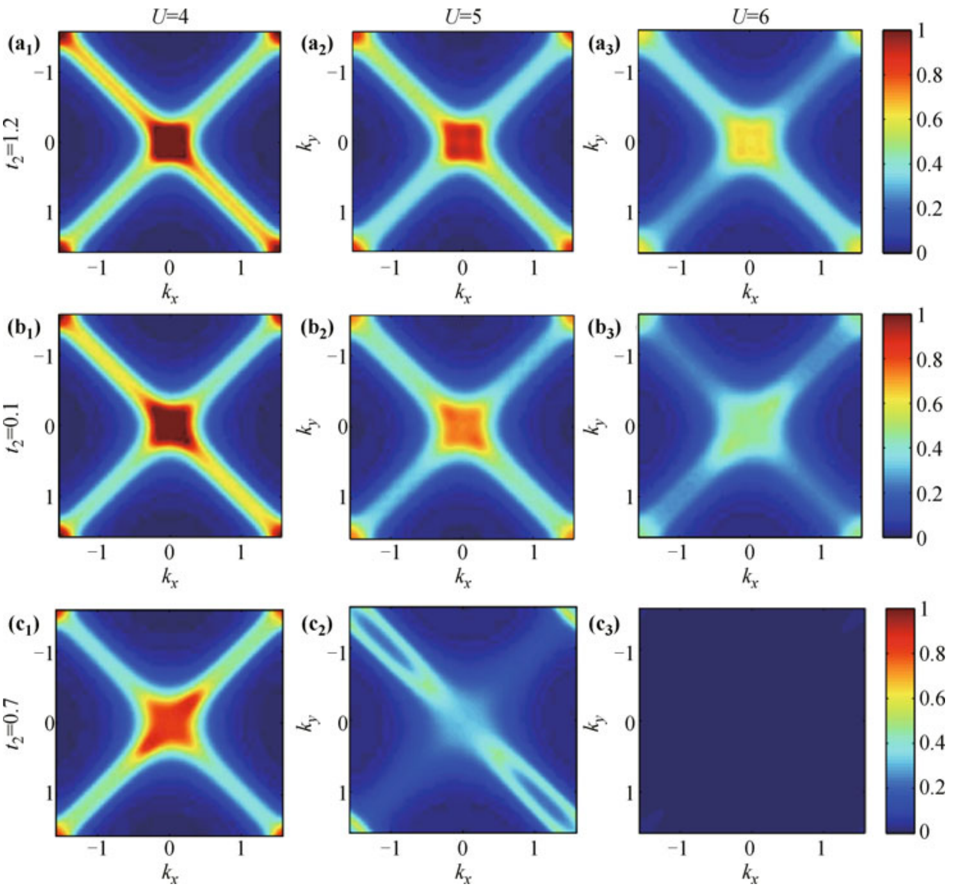

Fig. 19 The distribution of spectral weight $A(k,\omega=0)$ for different U at $T=0.1$. **(a)** $t_2=1.2$, **(b)** $t_2=1.0$, and **(c)** $t_2=0.7$. Peaks in the diagrams represent the dominating distribution of electrons with zero energy in momentum space and thus correspond to the location of Fermi surface. When the effect of interaction is small, it behaves like sharp peaks on the two diagonals in the first Brillouin zone, reflecting the Fermi surface at half-filling. With the increase of on-site repulsive interaction U and decreasing t_2, the renormalization effect becomes stronger, and the distribution spread. In (c3) where Mott transition occurs and the system is in the antiferromagnetic phase, no clear patterns of the distribution can be seen. Reproduced from Ref. [31].

is a large region in the parameter space where the RVB spin liquid state is favored. When $U>U_c$, a finite m means that the system is in a ferrimagnetic state. The inset in Fig. 21 shows the evolution of a single-particle energy gap ΔE at $\lambda=0.6$ and $T=0.5$, in which a gap opens at the A sites in advance.

For the decorated honeycomb lattice, we define an antiferromagnetic order parameter $m=(1/N_{\rm c})\sum_i sgn(i)(n_{i\uparrow}-n_{i\downarrow})$, where $\operatorname{sgn}(i)=1$ for $i=$ a$_1$, a$_3$(b$_3$), and b$_2$, and $\operatorname{sgn}(i)=-1$ for $i=$ b$_1$, b$_3$(a$_3$), and a$_2$.

To discuss the magnetic order in each state of a Shastry–Sutherl and lattice, we define the staggered magnetic order parameter $m=(1/N_{\rm c})\sum_i \operatorname{sgn}(i)(n_{i\uparrow}-n_{i\downarrow})$, where $\operatorname{sgn}(i)=1$ if $i=1$, 3 and $\operatorname{sgn}(i)=-1$ if $i=2$, 4, as shown in Fig. 6(b). The magnetic orders found in the Shastry–Sutherl and lattice as well as the evolution of the staggered magnetic order parameter m and the single-particle gap ΔE as a function of U for $T=0.1$ with $t_2=1.0$ are shown in Fig. 23. When $U=6$, both m and ΔE vanish and the system is in a paramagnetic metal phase. When $6<U<8$, the magnetic order forms while the single-particle excitation is still gapless, indicating that the system is in an antiferromagnetic metal phase. When U increases to 8, a gap opens and the system goes into an antiferromagnetic insulator phase. The inset in Fig. 23 shows that when $t_2=1.4$, there is only the metal–insulator transition at $U=10$ and all magnetic orders are suppressed due to strong frustration.

For the square–octagon lattice, we define an antiferromagnetic order parameter $m=(1/N_{\rm c})\sum_i \operatorname{sgn}(i)(n_{i\uparrow}-n_{i\downarrow})$, where $\operatorname{sgn}(i)=1$ if $i=1$, 3 and $\operatorname{sgn}(i)=-1$ if $i=2$, 4, as shown in Fig. 7(a). The magnetic orders found in the square–octagon lattice are shown in Fig. 24, and the evolution of m and ΔE as a

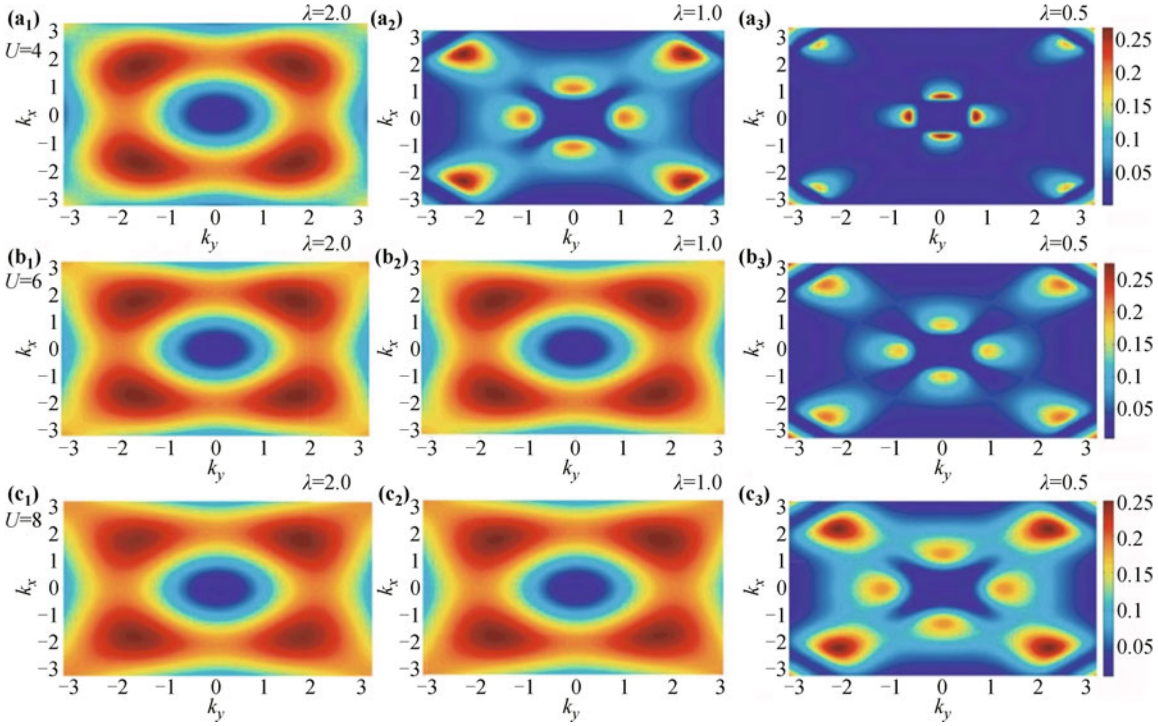

Fig. 20 Pictures in the same row depict the Fermi surface evolution for certain fixed on-site repulsive interaction and different anisotropic parameters while the pictures in the same column shows the Fermi surface evolution for certain fixed anisotropic parameter and different on-site repulsive interaction. Peaks in the diagrams represent the dominant spectral weight of electrons with zero energy in momentum space and thus correspond to the location of Fermi surface. With the increase of U and λ, the renormalization effect becomes stronger and the distribution spread. Fermi surface evolution is obtained at temperature $T/t_1 = 0.1$. Reproduced from Ref. [32].

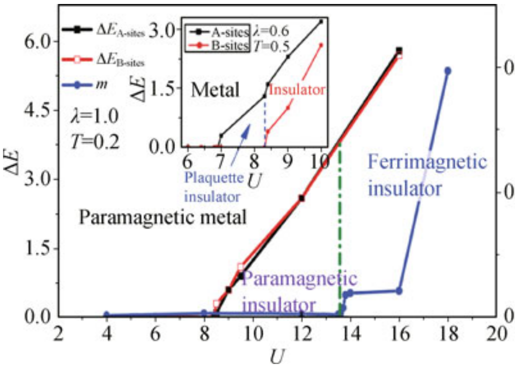

Fig. 21 The evolution of single particle gap ΔE and ferrimagnetic order parameter m for $\lambda = 1$ and $T = 0.2$. Paramagnetic metallic phase with $\Delta E = 0$ and $m = 0$ is found when U is weak. As U increases, a gap is opened and non-magnetic order is formed with $\Delta E \neq 0$ and $m = 0$. This paramagnetic insulating state can be a short range RVB spin liquid. An obvious magnetic order is formed when U is strong enough with $\Delta E \neq 0$ and $m \neq 0$. The inset picture shows the evolution of ΔE at $\lambda = 0.6$ and $T = 0.5$. A plaquette insulator is found when the A sites are insulating and the B sites are metallic. Reproduced from Ref. [28].

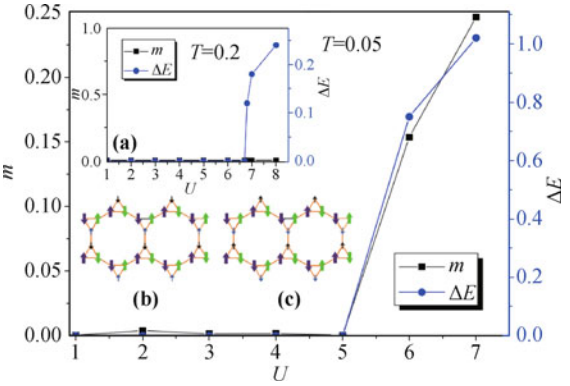

Fig. 22 Evolution of the antiferromagnetic order parameter m and the single-particle gap ΔE as a function of on-site repulsive interaction U for $\lambda = 1.0$ and $T = 0.05$. Insets: **(a)** Evolution of m and ΔE as a function of on-site repulsive interaction U for $\lambda = 1.0$ and $T = 0.2$; **(b)** and **(c)** two equivalent antiferromagnetic spin configurations of the antiferromagnetic insulator in a decorated honeycomb lattice. Reproduced from Ref. [43].

function of U for $T = 0.1$ is presented in Fig. 25.

Based on the density of states (or the momentum-resolved spectrum), the double occupancy, the evolution of the spectral function on a Fermi surface as a function of k, and the magnetic order parameters, we next present rich phase diagrams of temperature vs. interaction for the two-dimensional lattices.

The T–U phase diagrams of the TKL, half-filled with fermions, at $\lambda = 0.6$ and $\lambda = 0.1$ are shown in Fig. 26. The asymmetry which induced by different hoppings

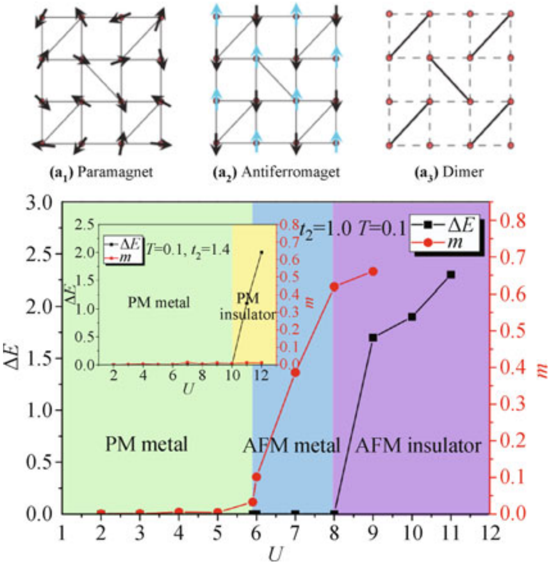

Fig. 23 Evolution of the staggered magnetic order parameter m and the single-particle energy gap ΔE as a function of on-site repulsive interaction U at $T = 0.1$ and $t_2 = 1.0$. When the interaction is weak, $\Delta E = 0$ and $m = 0$, and the system is in a paramagnetic (PM) metal phase. With the increase of the on-site repulsive interaction U, an antiferromagnetic (AFM) metal phase found with $m \neq 0$ but $\Delta E = 0$. When on-site repulsive interaction U is strong enough, both m and ΔE are not equal to zero, and the system enters anantiferromagnetic (AFM) insulator phase. The insert picture is for $t_2 = 1.4$. Reproduced from Ref. [31].

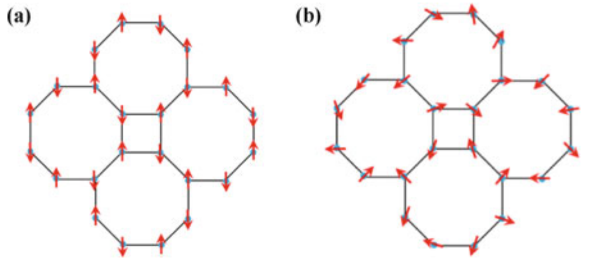

Fig. 24 **(a)** Sketch map of the anti-ferromagnetic order of square-octagon lattice. **(b)** Sketch map of the paramagnetic order of square-octagon lattice.

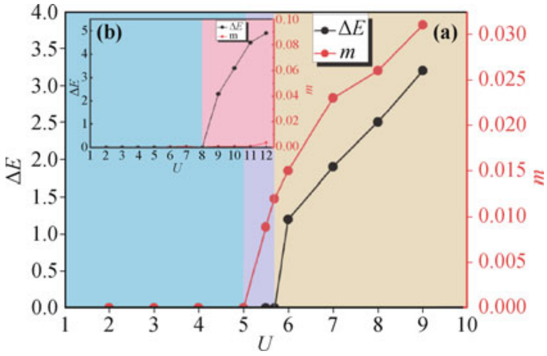

Fig. 25 **(a)** is the relationship between energy gap and on-site repulsive interaction for $T = 0.1$ while **(b)** for $T = 0.5$. For $T = 0.1$, antiferromagnetic state appears before the appearance of insulating state while the antiferromagnetic state disappears at $T = 0.5$. The right vertical axes in (a) and (b) shows the value of magnetic order parameter in each state. Reproduced from Ref. [32].

between two sublattices causes the phase transition points of the A and B sites to separate. As U increases, at $T = 0.5$ the A sites transition from a metallic phase into an insulating phase but the B sites stay in the plaquette insulating phase, in which electrons are localized at the A sites and the absence of next-nearest-neighbor hopping causes them to be itinerant only within the B sites. When $T < 0.34$, the B sites transition into Kondo metal state but the A sites remain in the metallic phase (see Fig. 26). This coexistence of phases corresponds to a Kondo metal, i.e., the localized electrons at the B sites act as the magnetic impurity, while the electrons at the A sites are still highly itinerant. In this situation, the system shows a strong Kondo effect because of the high density of magnetic impurities. When $U > U_c$, i.e., $U_c = 7.8$ at $T = 0.25$, both A and B sites transform into insulators. In Fig. 26, the A sites reenter the Mott transition because of frustration and asymmetry. This reentrant behavior, which is also found in the anisotropic triangular lattice, divides the coexisting phases into two parts: the plaquette insulator and the Kondo metal. The inset in Fig. 26 shows the phase diagram of the TKL at $\lambda = 1$. There are no coexisting phases or reentrant behavior when asymmetry is absent.

The finite-temperature phase diagrams of the isotropic decorated honeycomb lattice ($t' = t$), obtained from 6-site cluster and 12-sitecluster analyses show cluster-size dependence. At low temperatures, such as $T < T_{c1} \sim 0.1$, three phases are formed at different interaction strengths U. When $U < U_{c1} \sim 3.4$ at $T = 0.05$, the system is a semimetal (SM). In this phase, two Dirac points of the system have been broken away from the quadratic band crossing point and the low-energy physics is that of the

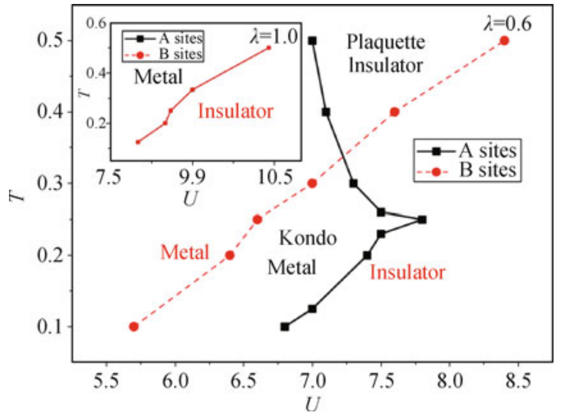

Fig. 26 Phase diagram of the TKL at $\lambda = 0.6$. The black solid lines show the transition line of the A sites, and the red dashed lines show the transition line of the B sites. Two kinds of coexisting phases between red lines and black lines are the plaquette insulator and Kondo metal. Inset: The phase diagram of the symmetric TKL ($\lambda = 1$), in which there are no-coexisting phases. Reproduced from Ref. [28].

Dirac fermion. When $U > U_{c2} \sim 5.2$ and $T = 0.05$, the system undergoes a first-order phase transition into a Mott insulator phase with antiferromagnetic order; this is called the antiferromagnetic insulator (AFI) phase. A nematic metal (NM) emerges at an intermediate interaction region, $U_{c1} < U < U_{c2}$, where U_{c1} and U_{c2} are the critical points of the SM–NM crossover and the NM–AFI phase transition, respectively. In this region, the system is metallic, has an anisotropic momentum-resolved single-particle spectrum at the Fermi level, and shows conventional Fermi-liquid behavior. With increasing temperature, the nematic order on the metal side and antiferromagnetic order on the insulator side are gradually destroyed by thermal fluctuation. The critical points (U_{c1}, T_{c1}) and (U_{c2}, T_{c2}), which indicate where the nematic order (green line with circles) and antiferromagnetic order phases (black lines with squares)break, are calculated. At very high temperatures, such as $T > T_{c1} = 0.13$, both the nematic order and the antiferromagnetic order are broken by thermal fluctuation, and the system goes from SM crossover to paramagnetic insulator with increasing interaction. As Fig. 27 shows that at $T = 0.15$, the system isa SM when $U < 6.2$ and a paramagnetic insulator when $U > 6.2$. For the 12-sitecluster, the properties of this system do not change but there is a slight shift in the phase boundary. For example, at $= 1/20$, the phase transition from to NM occurs at $U = 3.2$ ($U = 3.4$ for the 6-site cluster) and the NM-to-AFI transition occurs at $U = 5.0$ ($U = 5.2$ for the 6-site cluster).

We also obtained the T–U phase diagram for the Shastry–Sutherl and lattice while $t_2 = 1.0$ (Fig. 28). The antiferromagnetic metal phase exists when $T < 0.175$, and there is a phase transition from antiferromagnetic metal to AFI as U increases. When the temperature is high, magnetic orders are suppressed by thermal fluctuations and the system undergoes a transition from a paramagnetic metal phase to a paramagnetic insulator phase with increasing U. In addition, the inset of Fig. 28 shows the phase diagram with frustration for $t_2 = 1.3$. Because of strong frustration, magnetic orders are totally suppressed, even at low temperature, and both the AFM metal phase and the AFM insulator phase disappear. The only transition is from a PM metal to a PM insulator as U increases.

In the T–U phase diagram for the square–octagon lattice (Fig. 29), the system transitions from the paramagnetic metal state to the antiferromagnetic metal state at low temperature and weak interaction. The narrowness

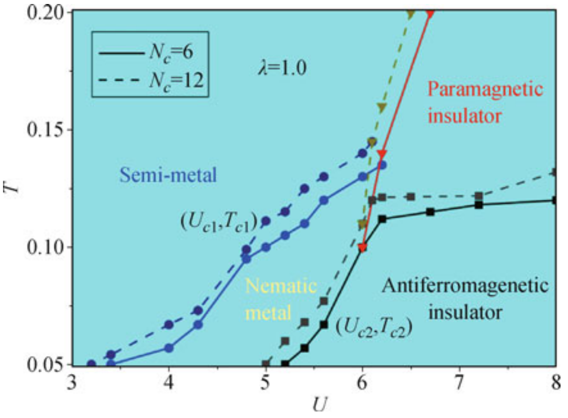

Fig. 27 Phase diagram of isotropic hopping ($\lambda = 1.0$) decorated honeycomb lattice. Solid and dashed lines are the results obtained using the6-site cluster ($N_c = 6$) and 12-site cluster ($N_c = 12$), respectively. Four phases in the phase diagram: (i) semi-metal (SM); (ii) antiferromagnetic insulator (AFI); (iii) Nematic metal (NM) and (iv) paramagnetic insulator (PM). The critical on-site repulsive interaction and critical temperature for SM-NM crossover are shown by (U_{c1}, T_{c1}). Critical points for the phase transition to AFI are shown as (U_{c2}, T_{c2}). Reproduced from Ref. [43].

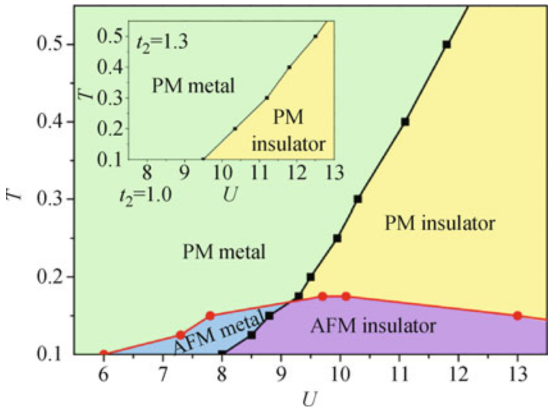

Fig. 28 T–U Phase diagram of interacting fermions on the Shastry–Sutherland lattice at $t_2 = 1.0$. The black line is the boundary between metal and insulator while the red line shows the transition from the paramagnetic (PM) phase to the antiferromagnetic (AFM) phase. There is a region of antiferromagnetic metal phase before the system enters the antiferromagnetic insulator phase at low enough temperature with the increase of U, The insert picture is for the case of $t_2 = 1.3$. Reproduced from Ref. [31].

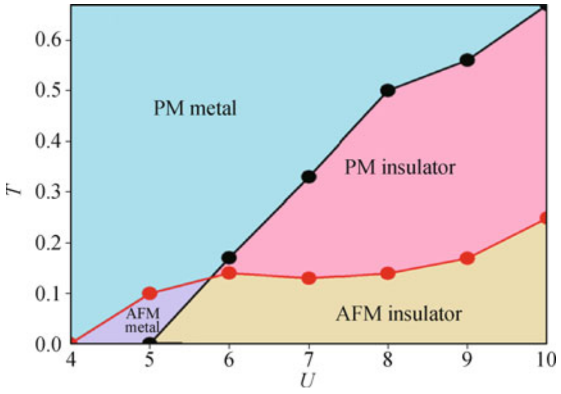

Fig. 29 T–U phase diagrams of isotropic square-octagon lattice for $\lambda = 1.0$. The black line is the boundary between metallic phase and insulating phase while the red one distinguishes the paramagnetic (PM) phase and anti-ferromagnetic (AFM) phase. Reproduced from Ref. [32].

of the antiferromagnetic metal state region means that this state is sensitive to temperature and on-site repulsive interaction. As the on-site repulsive interaction increases, the system transitions into the AFM insulator state.

In addition to the T–U phase diagram, we must discuss the competition between the anisotropic (asymmetry) parameter and the on-site repulsive interaction in these two-dimensional lattice systems. The definition of asymmetry in the TKL is when $\lambda = t_{ab}/t_{bb}$, where t_{ab} is the term for hopping between site $a$and site b and t_{bb} indicates hopping between the nearest-neighbor b sites. As λ increases, a zone in which the plaquette insulator and the Kondo metal coexist appears. This zone is suppressed in the range $\lambda = 0.9 - 1.11$. When $U > U_c$, such as $U_c = 13.8$, at $\lambda = 1$ the system becomes a ferromagnetic insulator with $m \neq 0$. Before entering the ferromagnetic phase, there is a paramagnetic insulator state. We argue this paramagnetic insulator state is a candidate for a short-range RVB spin liquid because of the absence of any magnetic order and long-range correlations.

Next, we investigate the influence of the lattice anisotropy, $\lambda = t'/t$, on phase transitions in the decorated honeycomb lattice. For $\lambda < 1$, the effective hopping amplitudes on vertex triangles are larger than those between vertex triangles and the electrons are more itinerant in the intra-triangles. For $\lambda > 1$, the effective hopping amplitudes on vertex triangles is smaller than those between vertex triangles and the electrons are more itinerant in the inter-triangles. When $\lambda = 1$, the NM phase is enhanced. Figure 31 shows the phase diagram in the λ vs. U plane when $T = 0.067$, for 6-site and 12-site clusters. The phase boundary is shifted by λ and the NM phase region gets larger as λ varies; thus, the nematic metal becomes more stable due to the enhanced anisotropy.

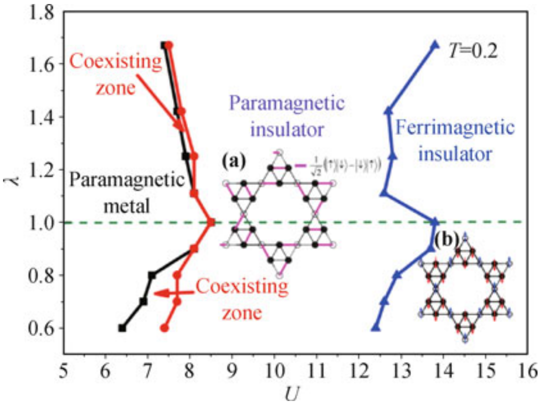

Fig. 30 The competition between U and λ in TKL at $T = 0.2$. The region between the black lines and the red lines denotes the coexisting zone which contains the plaquette insulator and the Kondo metal parts. A wide paramagnetic insulating region is found with an intermediate U. The blue lines show the transition point to the ferromagnetic insulator with a clear magnetic order. Inset: **(a)** One possible dimer configuration formed in the paramagnetic insulator, which is a candidate for the short range RVB spin liquid. **(b)** Spin configuration of ferrimagnetic insulator. Reproduced from Ref. [28].

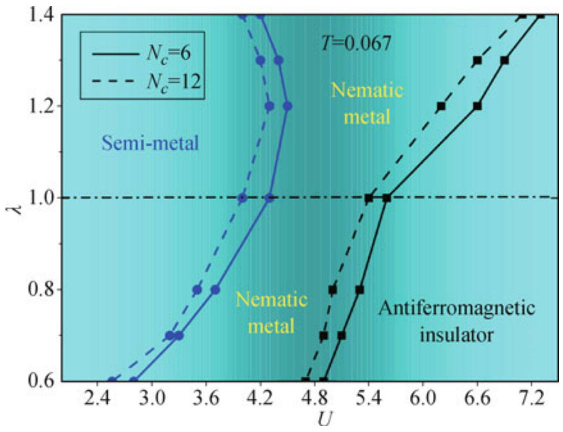

Fig. 31 Competition between on-site repulsive interaction anisotropic parameter λ in decorated honeycomb lattice when $T = 0.067$. Solid and dashed lines are the results obtained using the 6-site cluster ($N_c = 6$) and 12-site cluster ($N_c = 12$), respectively. Leftmost (blue) lines show the phase crossover line of the semimetal and Nematic metal; circles indicate critical points. Rightmost (black) lines show the phase translation line of the Nematic metal and antiferromagnetic insulator; squares indicate critical points. Reproduced from Ref. [43].

The competition between frustration and on-site repulsive interaction in the Shastry–Sutherl and lattice is shown in Fig. 32. When $t_2 = 0$, the Shastry–Sutherl and lattice transforms into a square lattice that is unstable toward an antiferromagnetic phase for an arbitrarily small interaction due to the perfect nesting of the Fermi surface, and the magnetic order is always accompanied by a Mott insulating gap. Figure 32 shows that the finite critical U is around 2.9 when $t_2 = 0$ because of the finite

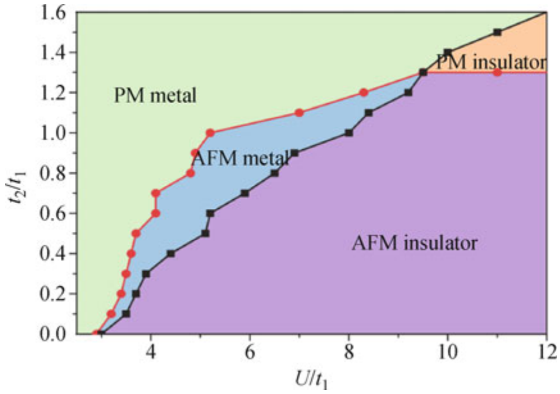

Fig. 32 $t_2 - U$ phase diagram at $T = 0.1$. When $t_2 < 1.3$, there is an antiferromagnetic metal phase between the paramagnetic metal phase and antiferromagnetic insulator phase. When $t_2 > 1.3$, a low-temperature paramagnetic insulator phase emerges (which should consist of a small plaquette phase and a dimer phase). eproduced from Ref. [31].

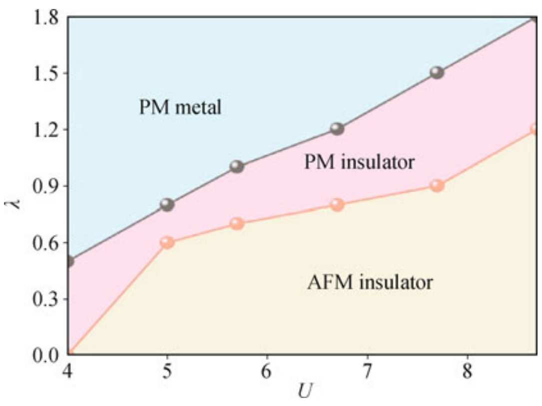

Fig. 33 $\lambda-U$ phase diagram at $T=0.17$. Reproduced from Ref. [32].

temperature. In the presence of frustration, instead of going directly into the AFM insulator phase from the PM metal phase when U increases, the system first enters an AFM metal phase. This shows that frustration plays an important role in the formation of an AFM metal. When $t_2=1.3$, the AFM metal phase disappears and a PM insulator phase emerges at $U=9.5$. The critical frustration $t_2=1.3$ obtained here is consistent with that obtained from the calculations of the two-dimensional Heisenberg model of the Shastry–Sutherl and lattice, beyond which the system was shown to consist of a small plaquette phase and a dimer phase.

Figure 33 shows the competition between λ and U at $T=0.17$ for the square–octagon lattice with strongly correlated fermions. The antiferromagnetic metal state disappears because of the competition but the other phases continue to exist at $T=0.17$.

4 Summary

Investigation of quantum phase transitions in two-dimensional lattices containing strongly correlated fermions is an important branch of condensed matter physics. First, in this review we introduced in detail the cellular dynamical mean-field theory and the continuous-time quantum Monte Carlo method, which we used in our work on the quantum phase transitions in two-dimensional lattices. Second, we presented magnetic quantum phase diagrams, including the T–U phase diagram, and the competition between the anisotropy (or asymmetry) parameter and on-site repulsive interaction in two-dimensional systems.

Acknowledgements I am so grateful for the great contributions and beneficial communications from Yao-Hua Chen, Hai-Di Liu, and Heng-Fu Lin while I am preparing this review paper. This work was supported by the National Science Foundation of China (Grant Nos. 11174169, 11234007, and 51471093).

References

1. T. Pruschke, M. Jarrell, and J. Freericks, Anomalous normal-state properties of high-T_c superconductors: Intrinsic properties of strongly correlated electron systems, *Adv. Phys.* 44(2), 187 (1995)
2. P. Fendley and K. Schoutens, Exact results for strongly correlated fermions in 2+1 dimensions, *Phys. Rev. Lett.* 95(4), 046403 (2005)
3. W. Krauth, M. Caffarel, and J. P. Bouchaud, Gutzwiller wave function for a model of strongly interacting bosons, *Phys. Rev. B* 45(6), 3137 (1992)
4. M. Hettler, A. N. Tahvildar-Zadeh, M. Jarrell, T. Pruschke, and H. R. Krishnamurthy, Nonlocal dynamical correlations of strongly interacting electron systems, *Phys. Rev. B* 58(12), R7475 (1998)
5. K. M. O'Hara, et al., Observation of a strongly interacting degenerate Fermi gas of atoms, *Science* 298, 2179 (2002)
6. E. Haller, R. Hart, M. J. Mark, J. G. Danzl, L. Reichsöllner, M. Gustavsson, M. Dalmonte, G. Pupillo, and H. C. Nägerl, Pinning quantum phase transition for a Luttinger liquid of strongly interacting bosons, *Nature* 466(7306), 597 (2010)
7. M. Capone, et al., Strongly correlated superconductivity, *Science* 296, 2364 (2002)
8. A. Georges, G. Kotliar, and Q. Si, Strongly correlated systems in infinite dimensions and their zero dimensional counterparts, *Int. J. Mod. Phys. B* 06(05n06), 705 (1992)
9. A. Ramirez, Strongly geometrically frustrated magnets, *Annu. Rev. Mater. Sci.* 24(1), 453 (1994)
10. Y. Yang and C. Thompson, Thermodynamics of the strongly correlated Hubbard model, *J. Phys. Math. Gen.* 24(6), L279 (1991)
11. J. H. Wu, R. Qi, A. C. Ji, and W. M. Liu, Quantum tunneling of ultracold atoms in optical traps, *Front. Phys.* 9(2), 137 (2014)
12. S. W. Song, L. Wen, C. F. Liu, S. C. Gou, and W. M. Liu, Ground states, solitons and spin textures in spin-1 Bose–Einstein condensates, *Front. Phys.* 8(3), 302 (2013)
13. A. Lüscher and A. M. Läuchli, Exact diagonalization study of the antiferromagnetic spin-1/2 Heisenberg model on the square lattice in a magnetic field, *Phys. Rev. B* 79(19), 195102 (2009)
14. D. Betts, H. Lin, and J. Flynn, Improved finite-lattice estimates of the properties of two quantum spin models on the infinite square lattice, *Can. J. Phys.* 77(5), 353 (1999)
15. C. C. Chang and R. T. Scalettar, Quantum disordered phase near the Mott transition in the staggered-flux Hubbard model on a square lattice, *Phys. Rev. Lett.* 109(2), 026404 (2012)
16. Y. H. Chen, J. Li, and C. S. Ting, Topological phase transitions with non-Abelian gauge potentials on square lattices, *Phys. Rev. B* 88(19), 195130 (2013)
17. D. Zanchi and H. Schulz, Weakly correlated electrons on a square lattice: Renormalization-group theory, *Phys. Rev. B* 61(20), 13609 (2000)

18. K. Takeda, N. Uryû, K. Ubukoshi, and K. Hirakawa, Critical exponents in the frustrated Heisenberg antiferromagnet with layered-triangular lattice: VBr2, *J. Phys. Soc. Jpn.* 55(3), 727 (1986)
19. K. Aryanpour, W. E. Pickett, and R. T. Scalettar, Dynamical mean-field study of the Mott transition in the half-filled Hubbard model on a triangular lattice, *Phys. Rev. B* 74(8), 085117 (2006)
20. T. Ohashi, T. Momoi, H. Tsunetsugu, and N. Kawakami, Finite temperature Mott transition in Hubbard model on anisotropic triangular lattice, *Phys. Rev. Lett.* 100(7), 076402 (2008)
21. T. Yoshioka, A. Koga, and N. Kawakami, Quantum phase transitions in the Hubbard model on a triangular lattice, *Phys. Rev. Lett.* 103(3), 036401 (2009)
22. A. Bao, Y. H. Chen, and X. Z. Zhang, Quantum phase transitions of fermionic atomsin an anisotropic triangular optical lattice., *Chin. Phys. B* 22(11), 110309 (2013)
23. T. Itou, A. Oyamada, S. Maegawa, M. Tamura, and R. Kato, Quantum spin liquid in the spin-1/2 triangular antiferromagnet EtMe$_3$Sb[Pd(dmit)$_2$]$_2$, *Phys. Rev. B* 77(10), 104413 (2008)
24. Y. Shimizu, K. Miyagawa, K. Kanoda, M. Maesato, and G. Saito, Spin liquid state in an organic Mott insulator with a triangular lattice, *Phys. Rev. Lett.* 91(10), 107001 (2003)
25. D. X. Yao, Y. L. Loh, E. W. Carlson, and M. Ma, XXZ and Ising spins on the triangular Kagome lattice, *Phys. Rev. B* 78(2), 024428 (2008)
26. Y. L. Loh, D. X. Yao, and E. W. Carlson, Dimers on the triangular Kagome lattice, *Phys. Rev. B* 78(22), 224410 (2008)
27. J. Zheng and G. Sun, Exact results for Ising models on the triangular Kagomé lattice, *Phys. Rev. B* 71(5), 052408 (2005)
28. Y. H. Chen, H. S. Tao, D. X. Yao, and W. M. Liu, Kondo metal and ferrimagnetic insulator on the triangular Kagome lattice, *Phys. Rev. Lett.* 108(24), 246402 (2012)
29. Y. L. Loh, D. X. Yao, and E. W. Carlson, Thermodynamics of Ising spins on the triangular Kagome lattice: Exact analytical method and Monte Carlo simulations, *Phys. Rev. B* 77(13), 134402 (2008)
30. A. Rüegg, J. Wen, and G. A. Fiete, Topological insulators on the decorated honeycomb lattice, *Phys. Rev. B* 81(20), 205115 (2010)
31. H. D. Liu, et al., Antiferromagnetic metal and Mott transition on Shastry-Sutherland lattice, *Sci. Rep.* 4, 4829 (2014)
32. A. Bao, H. S. Tao, H. D. Liu, X. Z. Zhang, and W. M. Liu, Quantum magnetic phase transition in square-octagon lattice, *Sci. Rep.* 4, 6918 (2014)
33. M. Kargarian, and G. A. Fiete, Topological phases and phase transitions on the square-octagon lattice, *Phys. Rev. B* 82(8), 085106 (2010)
34. X. P. Liu, W. C. Chen, Y. F. Wang, and C. D. Gong, Topological quantum phase transitions on the kagome and square-octagon lattices, *J. Phys.: Condens. Matter* 25(30), 305602 (2013)
35. S. Maruti and L. W. ter Haar, Magnetic properties of the two-dimensional "triangles-in-triangles" Kagomé lattice Cu$_9$X$_2$(cpa)$_6$ (X=F,Cl,Br), *J. Appl. Phys.* 75(10), 5949 (1994)
36. M. Gonzalez, F. Cervantes-lee, and L. W. ter Haar, Structural and magnetic properties of the topologically novel 2-D material Cu$_9$F$_2$ cpa)$_6$: A triangulated Kagome - like hexagonal network of Cu(II) trimers interconnected by Cu(II) monomers, *Molecular Crystals and Liquid Crystals Science and Technology A: Molecular Crystals and Liquid Crystals* 233(1), 317 (1993)
37. L. Balents, Spin liquids in frustrated magnets, *Nature* 464(7286), 199 (2010)
38. M. P. Shores, B. M. Bartlett, and D. G. Nocera, Spin-frustrated organic-inorganic hybrids of Lindgrenite, *J. Am. Chem. Soc.* 127(51), 17986 (2005)
39. M. Sasaki, K. Hukushima, H. Yoshino, and H. Takayama, Scaling analysis of domain-wall free energy in the Edwards–Anderson Ising spin glass in a magnetic field, *Phys. Rev. Lett.* 99(13), 137202 (2007)
40. H. Kageyama, K. Yoshimura, R. Stern, N. V. Mushnikov, K. Onizuka, M. Kato, K. Kosuge, C. P. Slichter, T. Goto, and Y. Ueda, Exact Dimer ground state and quantized magnetization plateaus in the two-dimensional spin system SrCu$_2$(BO$_3$)$_2$, *Phys. Rev. Lett.* 82(15), 3168 (1999)
41. M. R. He, R. Yu, and J. Zhu, Reversible wurtzite-tetragonal reconstruction in ZnO(1010) surfaces, *Angew. Chem. Int. Ed. Engl.* 51(31), 7744 (2012)
42. M. R. He, R. Yu, and J. Zhu, Subangstrom profile imaging of relaxed ZnO(10$\bar{1}$0) surfaces., *Nano Lett.* 12(2), 704 (2012)
43. H. F. Lin, Y. H. Chen, H. D. Liu, H. S. Tao, and W. M. Liu, Mott transition and antiferromagnetism of cold fermions in the decorated honeycomb lattice, *Phys. Rev. A* 90(5), 053627 (2014)
44. C. J. Bolech, S. S. Kancharla, and G. Kotliar, Cellular dynamical mean-field theory for the one-dimensional extended Hubbard model, *Phys. Rev. B* 67(7), 075110 (2003)
45. K. Haule, Quantum Monte Carlo impurity solver for cluster dynamical mean-field theory and electronic structure calculations with adjustable cluster base, *Phys. Rev. B* 75(15), 155113 (2007)
46. T. Kita, T. Ohashi, and S. Suga, Spatial fluctuations of spin and orbital in two-orbital Hubbard model: cluster dynamical mean field study, *J. Phys. Conf. Ser.* 150(4), 042094 (2009)
47. G. Kotliar, S. Y. Savrasov, G. Pálsson, and G. Biroli, Cellular dynamical mean field approach to strongly correlated systems, *Phys. Rev. Lett.* 87(18), 186401 (2001)
48. B. Kyung, G. Kotliar, and A. M. S. Tremblay, Quantum Monte Carlo study of strongly correlated electrons: Cellular dynamical mean-field theory, *Phys. Rev. B* 73(20), 205106 (2006)
49. A. Lichtenstein and M. Katsnelson, Antiferromagnetism and d-wave superconductivity in cuprates: A cluster dynamical mean-field theory, *Phys. Rev. B* 62(14), R9283 (2000)

50. A. Liebsch, Correlated Dirac fermions on the honeycomb lattice studied within cluster dynamical mean field theory, *Phys. Rev. B* 83(3), 035113 (2011)
51. O. Parcollet, G. Biroli, and G. Kotliar, Cluster dynamical mean field analysis of the Mott transition, *Phys. Rev. Lett.* 92(22), 226402 (2004)
52. H. Park, K. Haule, and G. Kotliar, Cluster dynamical mean field theory of the Mott transition, *Phys. Rev. Lett.* 101(18), 186403 (2008)
53. H. S. Tao, Y. H. Chen, H. F. Lin, H. D. Liu, and W. M. Liu, Layer anti-ferromagnetism on bilayer honeycomb lattice, *Sci. Rep.* 4, 5367 (2014)
54. E. Gull, A. J. Millis, A. I. Lichtenstein, A. N. Rubtsov, M. Troyer, and P. Werner, Continuous-time Monte Carlo methods for quantum impurity models, *Rev. Mod. Phys.* 83(2), 349 (2011)
55. P. Kornilovitch, Continuous-time quantum Monte Carlo algorithm for the lattice polaron, *Phys. Rev. Lett.* 81(24), 5382 (1998)
56. A. N. Rubtsov, V. V. Savkin, and A. I. Lichtenstein, Continuous-time quantum Monte Carlo method for fermions, *Phys. Rev. B* 72(3), 035122 (2005)
57. P. Werner, A. Comanac, L. de' Medici, M. Troyer, and A. J. Millis, Continuous-time solver for quantum impurity models, *Phys. Rev. Lett.* 97(7), 076405 (2006)
58. J. Hubbard, The dielectric theory of electronic interactions in solids, *Proc. Phys. Soc. A* 68(11), 976 (1955)
59. J. Hubbard, The description of collective motions in terms of many-body perturbation theory, *Proc. Royal Soc. Math. Phys. Eng. Sci.* 240(1223), 539 (1957)
60. J. Hubbard, The description of collective motions in terms of many-body perturbation theory (II): The correlation energy of a free-electron gas, *Proc. Royal Soc. Math. Phys. Eng. Sci.* 243(1234), 336 (1958)
61. J. Hubbard, Calculation of partition functions, *Phys. Rev. Lett.* 3(2), 77 (1959)
62. J. Hubbard, Electron correlations in narrow energy bands, *Proc. Royal Soc. Math. Phys. Eng. Sci.* 276(1365), 238 (1963)
63. J. Hubbard, Electron correlations in narrow energy bands (III): An improved solution, *Proc. Royal Soc. Math. Phys. Eng. Sci.* 281(1386), 401 (1964)
64. M. Jarrell and J. E. Gubernatis, Bayesian inference and the analytic continuation of imaginary-time quantum Monte Carlo data, *Phys. Rep.* 269(3), 133 (1996)